CrossMark

REVIEW

Ceramic Top Coats of Plasma-Sprayed Thermal Barrier Coatings: Materials, Processes, and Properties

Emine Bakan[1] · Robert Vaßen[1] ID

Abstract The ceramic top coat has a major influence on the performance of the thermal barrier coating systems (TBCs). Yttria-partially-stabilized zirconia (YSZ) is the top coat material frequently used, and the major deposition processes of the YSZ top coat are atmospheric plasma spraying and electron beam physical vapor deposition. Recently, also new thermal spray processes such as suspension plasma spraying or plasma spray-physical vapor deposition have been intensively investigated for TBC top coat deposition. These new processes and particularly the different coating microstructures that can be deposited with them will be reviewed in this article. Furthermore, the properties and the intrinsic–extrinsic degradation mechanisms of the YSZ will be discussed. Following the TBC deposition processes and standard YSZ material, alternative ceramic materials such as perovskites and hexaaluminates will be summarized, while properties of pyrochlores with regard to their crystal structure will be discussed more in detail. The merits of the pyrochlores such as good CMAS resistance as well as their weaknesses, e.g., low fracture toughness, processability issues, will be outlined.

Keywords coatings for engine components · corrosion protection · segmented coatings · thermal barrier coatings (TBCs) · zirconia

✉ Robert Vaßen
r.vassen@fz-juelich.de

Emine Bakan
e.bakan@fz-juelich.de

[1] Forschungszentrum Jülich GmbH, Institute of Energy and Climate Research, Materials Synthesis and Processing (IEK-1), 52425 Jülich, Germany

Thermal Barrier Coatings

Thermal barrier coatings (TBCs) are protective coatings applied to the surface of hot metallic sections in gas turbine engines. The major fields of the application of gas turbines in which the TBCs are utilized are aircraft propulsion and power generation. In 2016, the market forecasters estimated an impressive production of nearly 228,000 aviation gas turbine engines valued in $1.232 trillion through 2030 and of 5480 power generation gas turbine engines worth $105.3 billion over the next 10 years (Ref 1, 2). Considering these figures, it is only rational to estimate a rising demand for the protective coating technologies in the near future.

The conventional TBCs systems consist of a ceramic top coat (1), a metallic bond coat (2), and a thermally grown oxide "TGO" layer (3) that forms due to oxidation of the bond coat as a result of oxygen inward diffusion through the top coat at TBC operation temperatures. The aluminum-rich bond coat ((Ni, Co)CrAlY or aluminides of Pt and Ni), which forms the alumina (α-Al_2O_3) TGO layer on top, has the primary function of protecting the substrate from oxidation. Providing the thermal insulation in the TBC system is the main function of the ceramic top coat layer. Since it was introduced in the 1970s (Ref 3), 6-8 wt.% yttria-stabilized zirconia (7YSZ) has been the material of choice for ceramic top coats, as it has the exceptional combination of desired properties ("Properties" section).

TBCs are complex systems bringing the metallic and ceramic materials together, to function under highly demanding thermal cycling conditions. To that end, ceramic materials are further enhanced in terms of both thermal insulation efficiency and thermal expansion compliance in different ways and extend by different processing routes.

APS and EB-PVD are two established methods, while newer thermal spray techniques such as suspension plasma spray (SPS) and plasma spray-physical vapor deposition (PS-PVD) are under development showing attractive properties ("Deposition Technologies and Microstructure" section).

Even though the 7YSZ remained as the state of the art for decades, its temperature limitation at about 1200 °C ("Degradation" section) has been the main motivation to modify it chemically or to substitute it with new ceramic materials to further boost engine efficiency. Therefore, new ceramic compositions were extensively studied, yet in many of these materials with high-temperature stability, other critical issues such as interdiffusion with alumina TGO and low fracture toughness were observed. This introduced the double ceramic layer concept to the TBC literature, combining the benefits of YSZ and new materials. Furthermore, deposition of several of these complex oxides with stoichiometric compositions was found to be not so easy with both thermal spray and vapor phase deposition processes, implying a demand for more careful process optimizations ("Alternative Ceramic Top Coat Materials" sections).

YSZ Ceramic Top Coat

Properties

A good thermal stability, a low thermal conductivity, a high coefficient of thermal expansion (CTE) in combination with a high fracture toughness are the main required properties for the ceramic top coat on top of metallic components. The YSZ has a high melting point (2700 °C) and one of the lowest thermal conductivities of all ceramics at elevated temperatures; the conductivity of bulk YSZ and YSZ coatings with different microstructures and porosity were reported to be 2.6 W/mK (5.3 wt.% YSZ, 600 °C) (Ref 4) and 0.7-1.4 W/mK (7.25 wt.% YSZ) (Ref 5), respectively. The YSZ also has a high CTE (11×10^{-6} K^{-1}), which is close to that of the underlying superalloy substrate (14×10^{-6} K^{-1}) (Ref 6) and helps to mitigate stresses arising from the thermal expansion mismatch. But a mismatch still remains and these stresses lead to crack propagation within the coatings regardless of the high toughness of 7 wt.% YSZ (phase composition and transitions will be elaborated below). Therefore, mainly by trying to reduce the stress levels and/or increasing the strain tolerance of the coatings, a further improvement of the coating performance is desired. This can be achieved by introducing porosity and cracks (interlamellar cracks, segmentation cracks, etc.) into the coatings or depositing columnar structures which will be discussed below.

Deposition Technologies and Microstructure

APS, SPS, and PS-PVD thermal spray technologies, as well as micro-cracked, segmented, and columnar coating microstructures that can be produced via these methods, will be reviewed in the following sections. As the focus is thermal spray technologies in this article, the EB-PVD process will not be discussed in detail and further information can be found, e.g., in Ref 7.

Atmospheric Plasma Spraying Process

In the APS process, an electric arc generated between anode and cathode ionizes the flowing process gasses (argon, hydrogen, nitrogen, or helium) into the plasma state (Fig. 1, left). The ceramic powder particles are injected into this plasma jet where they are heated and accelerated toward the substrate so that the molten or partly molten particles impact the surface of the substrate at high speed. This leads to deformation of the particles and spread like pancakes or so-called splats (1-5 μm thick, 200-400 μm diameter) (Ref 8, 9). Heat from the hot particles is transferred to the cooler substrate material, and the splats rapidly solidify and shrink. Due to hindered contraction of the splats on the substrate or on the previously deposited layer, tensile quenching stresses arise within the splats and mainly relaxed by micro-cracking (Ref 10). As a result of quenching stresses as well as imperfect splat contacts, a coating microstructure with typical intersplat, intra-splat cracks, and larger spherical pores is deposited on the substrate in the plasma spray process (Fig. 1, right). Such microstructure with 10-20 vol.% cumulative porosity lowers the thermal conductivity (in particular, the intersplat cracks aligned parallel to the substrate surface and normal to the heat flux, typical 0.7-1.0 W/m/K) and the elastic modulus of the ceramic top coat for a better thermal insulation and thermo-mechanical performance, respectively. Additionally, the micro-cracks allow partial sliding of the individual splats along their boundaries and a kind of stress release even at room temperature takes place by that process (Ref 11). Therefore, spray parameters such as spray torch power, plasma gas composition, and spray distance, which affect melting states and velocities of the particles, or temperature of the substrate determining the cooling rates of the splats on arrival are carefully tuned to achieve the desired porous microstructures. It should be also mentioned here that, other than the specific spraying conditions leading to high porosity levels, today it is well known to use plastic-ceramic powder mixtures for the same purpose (Ref 12, 13).

Figure 2 illustrates the stress development in a porous, micro-cracked coating, which is deposited on a superalloy substrate, during a thermal cycle. When this system is
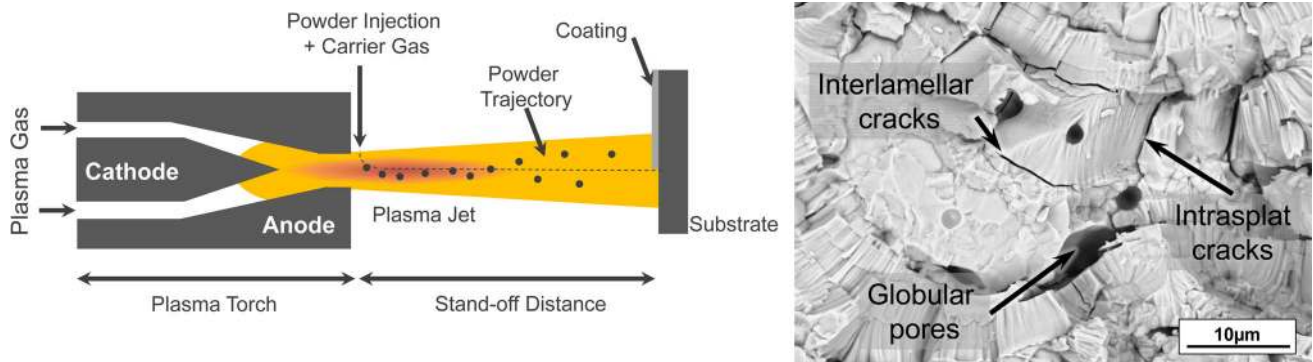
Fig. 1 Schematic of plasma spraying process with powder injection (left), fracture microstructure of a TBC sample deposited with the APS (right)

Fig. 2 Qualitative stress development within different TBCs deposited on a nickel base superalloy during heating (1), dwell time at temperature (2), cooling (3) and at room temperature (4)
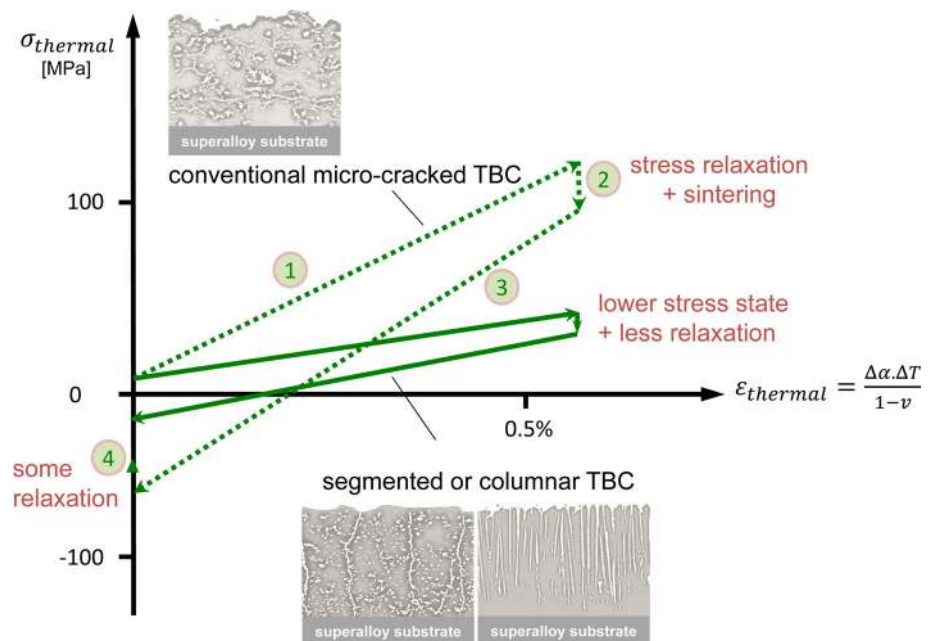
heated, tensile stresses develop in the coating (1) due to the larger thermal expansion coefficient of the substrate. At high temperature, stress relaxation and sintering of the coating take place, the former leading to a reduction of the thermal stress (2), the latter leading to a steeper slope during cooling (3). Both factors increase the compressive stress level at room temperature which might be slightly reduced by room temperature relaxation (4).

This stress development in the coatings becomes more critical if the thickness of the coating (d_{coat}) is desired to be as high as in the millimeter range. Because driving force for the crack propagation is the elastic energy stored in the coating and can be described by the energy release rate (G) (Ref 14).

$$G = \frac{(1-n^2)\sigma_{coat}^2 d_{coat}}{2(1-n)^2 E_{coat}} = \frac{(1-n^2)}{2(1-n)^2}\Delta\varepsilon^2 E_{coat} d_{coat} \quad \text{(Eq 1)}$$

For a given strain ($\Delta\varepsilon$), which is determined by the thermal expansion mismatch between coating and substrate and the relaxation at high temperatures, the energy release rate is proportional to the d_{coat} and inversely proportional to elastic modulus of the coating (E_{coat}) and an additional factor (n) which is a function of the Poisson's ratio (v). For that reason, a further increase in the porosity levels (>20%) of high-thickness coatings is required to lower the E_{coat} and as a result to obtain sufficiently low driving force for crack propagation.

Segmented Coating by Atmospheric Plasma Spraying

Another efficient way to reduce the energy release rate especially for thick coatings is the introduction of segmentation cracks, which are the vertical cracks running

perpendicular to the coating surface. These systems are also called as dense vertically cracked (DVC) TBCs, and they were developed more than 20 years ago (Ref 15). Vertical cracks can be formed in the top coat by specific, hot spray conditions which allow a good bonding between the splats and only limited micro-crack formation. As a result, large tensile stresses are developed in these dense coatings which relax by the formation of segmentation cracks with typical densities in the order of 3-10 cracks/ mm (Ref 16, 17). As shown in Fig. 2, the presence of these cracks significantly reduces the mean stress level in the coating by opening during heating period, and hence the relaxation at high temperature also becomes limited. Moreover, the already rather dense structure only shows limited further increase in the elastic modulus. However, due to dense structure, the thermal conductivity of these coatings is relatively high (typically 1.3-1.8 W/m/K) compared to their micro-cracked counterparts. Similarly, the columnar structure of EB-PVD coatings, which is obtained by the condensation of vaporized coating material on the surface of a heated substrate, exhibits a great strain tolerance (Fig. 2) but also a higher thermal conductivity due to the presence of columnar gaps (Ref 18). Therefore, generally, EB-PVD coatings are preferred because of their greater strain tolerance for the applications where frequent thermal cycling will occur, even though they are inferior to APS coatings regarding thermal insulation.

Segmented and Columnar Coatings by Suspension Plasma Spraying

Another thermal spray technology which can generate segmented coatings with a rather high porosity level is the SPS process (Ref 19). Here a suspension of submicron ceramic particles instead of the micron-sized feedstock powder is used. Also, precursors as metal salts have been employed [so-called solution precursor plasma spraying (SPPS) (Ref 20). The finer size of the deposited droplets allows the generation of different microstructures, especially a high segmentation crack density [even above 10 cracks/mm (Ref 21)] and a high cumulative porosity mainly consisting of sub-micrometer range pores (Ref 22)] (Fig. 3, left). As a result of this microstructure, the thermal conductivity of SPS coatings is in a similar range with that of APS porous coatings and lower than the one of APS segmented coatings. The thermal shock resistance and thermal cyclic performance of the SPS coatings can be excellent (Ref 23, 24). Recently, it also was discovered that the SPS process allows the formation of columnar structures. Under certain process conditions, the fine droplets will follow the process gas flow parallel to the surface of the substrate and will impinge on obstacles leading to the formation of columns (Ref 25) (Fig. 3, right). Also, these coatings can show excellent thermal cycling performance (Ref 26) and additionally a non-line of sight capacity which is favorable for the coating of complex shaped components. In the last years, the SPS process has also successfully been used to deposit different thermal barrier coating materials like perovskites (Ref 21) and pyrochlores (Ref 27) as segmented or columnar structured coatings.

### Columnar Coatings by Plasma Spray Physical Vapor Deposition

A rather new thermal spray technology is the plasma spray physical vapor deposition. It uses a high-energy plasma gun operated in an inert atmosphere at reduced work pressures (50-200 Pa) which enables the vaporization of fine feedstock material and can produce columnar like structures by a vapor phase deposition similar to the EB-PVD process (Fig. 4). In addition to the high strain tolerance microstructure, the PS-PVD offers lower investment costs and higher deposition rates than the EB-PVD along with the ability of coating complex geometries and shadowed areas (Ref 28). This is possible due to the gas flow giving a non-line-of-sight characteristic. With the use of suitable feedstock materials, also other TBC materials can be processed by PS-PVD. As an example, $Gd_2Zr_2O_7$ coating deposited by the PS-PVD process was represented by Rezanka et al. (Ref 29) and lifetime of this coating in a $YSZ/Gd_2Zr_2O_7$ system was shown to be two times longer than the conventionally sprayed TBCs (see "Implementation Issues and Performance" section).

Degradation

The newer thermal spray technologies presenting highly strain tolerant and porous coatings seem already to surpass the capabilities of the APS. On the other hand, maintenance of strain tolerance and porosity requires the sintering resistance and phase stability of the top coat material at high application temperatures. Unfortunately, the YSZ shows accelerated sintering above 1200 °C and resultant improved intersplat bonding and micro-crack healing lowers the thermal resistance and increases the elastic modulus of the coating (Ref 30). Furthermore, its insufficient phase stability after long-term exposure at temperatures above 1200 °C affects the lifetime of the plasma-sprayed ceramic YSZ top coat undesirably. At room temperature, a non-equilibrium tetragonal phase (t', also called non-transformable tetragonal) is observed in the as-sprayed YSZ coatings. The t' phase is formed due to rapid cooling during the deposition process, which kinetically suppresses the formation of equilibrium phases (low-yttria containing transformable tetragonal and high-yttria containing cubic), and therefore, very small amounts of the equilibrium
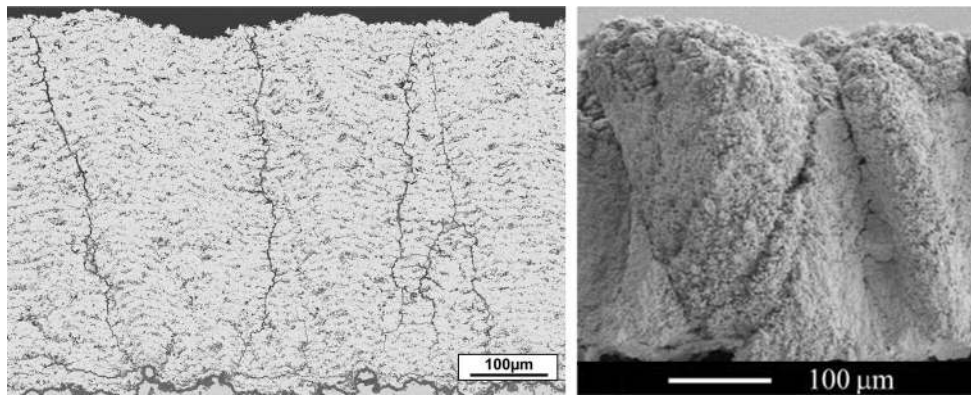
Fig. 3 Cross section of an as-sprayed SPS YSZ coating with segmentation cracks (left, Ref 22) and with columnar structure (right, Ref 25)
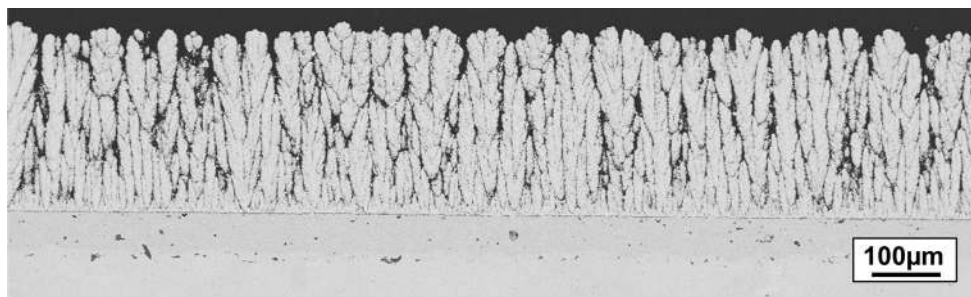
Fig. 4 Fracture surface of a columnar YSZ microstructure produced by PS-PVD (Ref 29)

phases are observed in the as-sprayed microstructures. However, the t' phase undergoes phase separations into the cubic and transformable tetragonal (t) phases at elevated temperatures. Primarily the cubic phase precipitates leading to depletion of yttria in t' phase, which results in the formation of the t phase, yet the mechanism of the transformation is still a subject of debate (Ref 31). In one of the early studies, the extent of the t' phase separation was reported to be comparable after 100 h aging at 1200 °C and after 1 h aging at 1400 °C (Ref 32). Upon cooling after aging at these temperatures, the cubic phase is maintained, whereas tetragonal phase may experience the tetragonal to monoclinic martensitic transformation ($t \leftrightarrow m$). The cubic phase is not desired in the TBCs due to its low fracture toughness (20 wt.% YSZ, $K_c \sim 1$ MPam$^{0.5}$) that leads to inferior thermal cycling lifetime in comparison with the t' phase, which exhibits higher toughness owing to ferroelastic domain switching mechanism (7 wt.% YSZ, $K_c \sim 3$ MPam$^{0.5}$) (Ref 33, 34). The martensitic transformation of the t phase is also detrimental for thermal cycling lifetime on account of accompanied volume change ($\sim 4\%$) (Ref 35). Therefore, alternative stabilizers to yttria such as CeO$_2$ (Ref 36), or additions to YSZ such as Sc$_2$O$_3$ (Ref 37), TiO$_2$ (Ref 38), have been investigated to further increase the highest stability temperature of t' phase for advanced TBC applications (≥ 1400 °C). ZrO$_2$-YO$_{1.5}$-TaO$_{2.5}$ material

system similarly offers increased stability temperatures (1500 °C) and moreover reported to have somewhat higher fracture toughness values than the standard 7YSZ (Ref 39, 40).

Thermochemical compatibility of the components in the TBC system is another critical factor for the durability. Interactions between the TGO and ceramic top coat can result in replacing the alumina with less protective oxides and hence can be deleterious for the system. However, the solubility of YSZ (up to 20 wt.% yttria addition) and alumina in each other is reported to be very limited up to 1250 °C (Ref 41, 42).

In addition to intrinsic issues leading to degradation of the TBC system, there are also extrinsic degradation mechanisms such as erosion, FOD (foreign object damage), hot corrosion, and CMAS (initials of calcium-magnesium alumina-silicate) attack. Erosion and FOD are leading to the progressive loss of thickness and total coating removal, respectively (Ref 43). Small particles ingested into turbines and internally generated larger particles (such as engine wear residues, thermally spalled TBC from the combustor) contribute to erosion damage, while any foreign objects such as rocks, ice from the wings in case of FOD impact the components of the engine and can have disastrous consequences. Hot corrosion of TBC occurs due to molten deposits resulting from impurities in the fuel; the impurities

such as sodium, sulfur, vanadium, lead, and phosphorus are oxidized during combustion to form strong acidic or alkaline oxides that attack both the ceramic and metallic components of the TBC system. It was found that the Y_2O_3 in YSZ thermal barrier coatings reacts strongly with the V_2O_3 resulting in the formation of YVO_4, which depletes yttria from the zirconia matrix and causes the spallation of TBC (Ref 44). Different approaches were introduced to improve the corrosion resistance of YSZ such as altering the yttria content or the stabilizer of the zirconia matrix. Scandia-yttria-stabilized zirconia was found to be more corrosion resistant to vanadate hot corrosion, but also some stabilization issues of it were reported by Jones et al. (Ref 45).

A similar degradation mechanism at high operation temperatures is caused by the environmentally ingested airborne sand/ash particles melt on the hot TBC surfaces resulting in the deposition of the CMAS glass deposits (Ref 46-48). At high surface temperatures, the CMAS rapidly penetrates the porosity of the coating and lead to premature failure of it as a consequence of mechanical and chemical interactions. Former leads to loss of strain tolerance and stiffening of the YSZ coating, while the latter result in the destabilization of the YSZ. Due to the presence of the CMAS in the structure with much lower CTE than the YSZ top coat and metallic components, large compressive stresses develop upon cooling increasing further the energy release rate of the system. CMAS was also reported to lower the yttria content of the YSZ, which results in the formation of transformable monoclinic zirconia as discussed above and consequently compromising the integrity of the system (Ref 48). From a mechanical point of view, the CMAS-induced degradation relies on progressing of the molten deposits through the pores of the top coat surface. Therefore, the surface porosity of the top coat becomes critical and makes EB-PVD top coat microstructures particularly vulnerable to the CMAS attack. From a chemical perspective, Aygun et al. (Ref 49) showed that up to 20 mol.% Al_2O_3 and 5 mol.% TiO_2 additions into YSZ enable to mitigate CMAS attack by incorporation of both Al and Ti solutes within CMAS glass. Later, it was also shown that increasing the yttria content of zirconia increases the CMAS resistance (Ref 50) although other issues related to phase stability are manifested in that case.

Alternative Ceramic Top Coat Materials

Over the last 15 years, primarily four different ceramic material groups: (1) zirconia doped with different rare-earth (RE) cations (defect cluster TBC's), (2) perovskites, (3) hexaaluminates, and (4) pyrochlores have been suggested as promising new top coat materials (see Table 1 for the chemical compositions). Some other materials, e.g., mullite (Ref 51), silicates [$ZrSiO_4$ (Ref 6)], garnets [$Y_3Al_5O_{12}$ YAG (Ref 52), $Y_4Al_2O_9$ YAM (Ref 53)], $(Ca_{1-x}Mg_x)Zr_4(PO_4)_6$ (Ref 54), were also considered as candidate materials; however, their typically low CTE precludes the possibility of their application.

Defect Cluster TBCs

In defect cluster TBC's, the zirconia is doped with oxides of the different RE cations. Due to a significant difference between the ionic sizes of the zirconia and RE, a highly defective lattice is produced while thermodynamic stability can be preserved. The obtained lattice distortion scatters lattice and radiative photon waves and hence reduces the thermal conductivity of the material. Zhu et al. (Ref 55) reported that the thermal conductivity of the standard ZrO_2-4.5 mol.% Y_2O_3 could be reduced about 40% (from ~2.5 to 1.7 W/mK) when the zirconia doped with 5.5 mol.% Y_2O_3-2.25 mol.% Gd_2O_3-2.25 mol.% Yb_2O_3. Furthermore, good thermal cycling performances of the

Material group	Composition/example
Defect cluster zirconia	ZrO_2-Y_2O_3-Gd_2O_3-Yb_2O_3
Perovskites	Zirconates
	$AZrO_3$ (A = Sr, Ba, Ca)/$SrZrO_3$
	Complex forms
	ABO_3 (A = Ba, La, B = (paired Mg,Ta, Al, La)/$Ba(Mg_{1/3}Ta_{2/3})O_3$
Hexaaluminates	(La, Nd)$MAl_{11}O_{19}$ (M = Mg, Mn to Zn, Cr or Sm)/$LaMgAl_{11}O_{19}$
Pyrochlores	$A_2B_2O_7$
	A and B are 3 + or 2 + and 4 + or 5 + cations/$La_2Zr_2O_7$

Table 1 Composition of alternative top coat material groups

defect cluster zirconia with low dopant concentrations were observed. However, decreasing cyclic lifetimes were monitored when the dopant concentrations were increased due to reduced fraction of tetragonal phase and hence reduced toughness values (Ref 56).

Perovskites

The perovskites were considered as candidate materials mainly due to their refractory properties (melting point, $SrZrO_3$; 2650 °C, $Ba(Mg_{1/3}Ta_{2/3})O_3$; 3100 °C). Their CTE higher than 8.5×10^{-6} K^{-1} and thermal conductivity lower than 2.2 W/mK were also found to be advantageous for TBCs. However, later it was observed that complex perovskites (e.g., $Ba(Mg_{1/3}Ta_{2/3})O_3$, $La(Al_{1/4}Mg_{1/2}Ta_{1/4})O_3$) decompose during spraying and hence the deposit is often accompanied by secondary phases, while $SrZrO_3$ undergoes some phase transformations and the one from orthorhombic to pseudo-tetragonal which occurs at 740 °C involves a volume change of $\sim 0.14\%$ (Ref 57-59). Ma et al. reported that doping the $SrZrO_3$ with Yb_2O_3 and Gd_2O_3 not only suppresses the phase transformation but also lowers the thermal conductivity of $SrZrO_3$ ($\sim 20\%$). This modification also yields longer cyclic lifetimes than the standard YSZ particularly in a *double-layer* structure above 1300 °C (Ref 60).

The double-layer structure describes a two-layer ceramic coating system (YSZ and an alternative material on top of it with high-temperature stability such as perovskite and pyrochlore). The YSZ layer between the TGO and the alternative ceramic material was introduced to solve thermochemical incompatibility problems with the TGO but more often to take advantage of high toughness of the YSZ close to the TGO (Fig. 5). Therefore, today it is a well-accepted approach and successful examples combining different materials with the YSZ and using different deposition methods (APS, EB-PVD) can be found in the literature (Ref 60-64).

Hexaaluminates

Among the hexaaluminates, lanthanum hexaaluminate (LHA) with defective magnetoplumbite structure, which crystallizes in the form of plate-like grains, is the most investigated material for TBCs. Because in addition to a similar thermal conductivity to the YSZ (2.6 W/mK), it offers a low Young's modulus, significantly high sintering resistance, structural and thermochemical stability up to 1400 °C (Ref 65, 66). Furthermore, due to the amorphous content of the coatings made of different hexaaluminate compositions (particularly pronounced for $LaLiAl_{11}O_{18.5}$) in the as-sprayed state, formation of a segmentation crack network in the coatings was observed after heat treatments (Ref 67). As a result of this advantageous combination of properties, good cyclic lifetime performance of LHA was reported in the literature (Ref 68). More recently, another hexaaluminate $LaTi_2Al_9O_{19}$ was conceived as a novel TBC material (Ref 69) due to its low thermal conductivity (1.0-1.3 W/mK) and phase stability up to 1600 °C. The CTE of the $LaTi_2Al_9O_{19}$ was reported in the range of
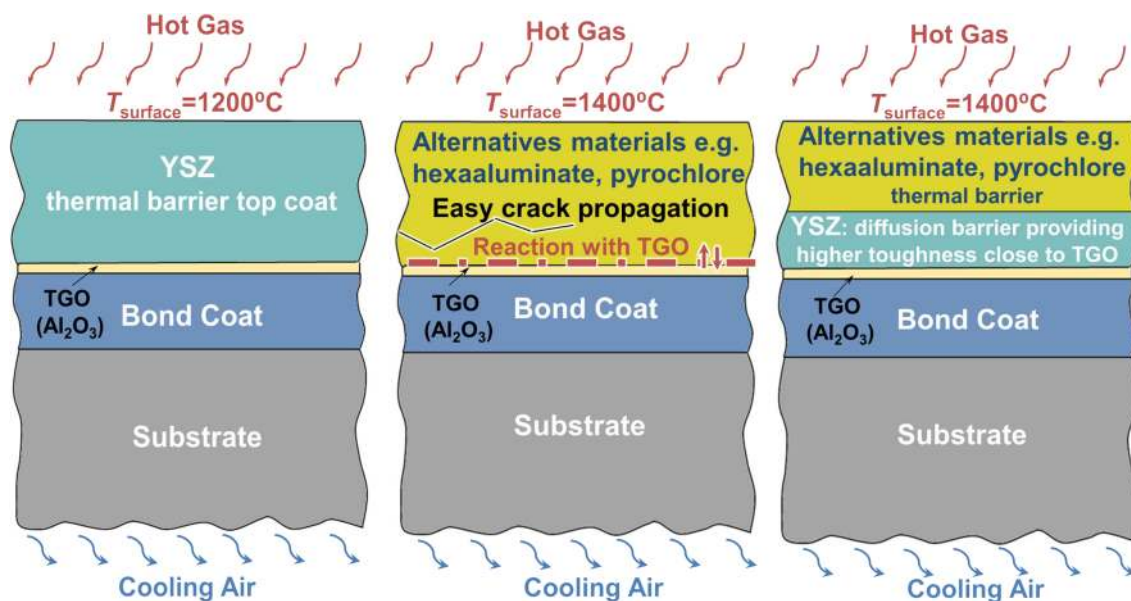
Fig. 5 Introducing the double-layer structure to the TBCs for higher operation temperatures; schematic illustration of a standard YSZ TBC with the max. temperature capability of 1200 °C (left), single-layer alternative material TBC with a higher temperature capability which suffers from easy crack propagation and interdiffusion with the TGO (middle), a double-layer TBC with a YSZ interlayer (right) (Ref 115)

8-12 × 10^{-6} K^{-1} (200-1400 °C), which is also comparable to that of the YSZ. Nevertheless, no significant improvement in the performance was monitored when the LaTi$_2$Al$_9$O$_{19}$ is implemented as a single layer (<200 cycles at 1300 °C) due to its low fracture toughness. However, the performance was significantly advanced in a double-layer system (1375 cycles at 1300 °C).

Pyrochlores

According to Web of Science, among the four aforementioned material groups, the most extensively investigated group for TBCs is the pyrochlores. Figure 6 demonstrates the significant increase in the number of the publications covering the pyrochlores within the years in comparison with its counterparts. The increasing popularity of the pyrochlores can be justified with their good combination of properties such as low thermal conductivity and high-temperature phase stability but mostly with their pronounced CMAS resistance. These properties of pyrochlores with regard to their crystal structure as well as some implementation issues will be discussed more in detail below.

Crystal Structure

The pyrochlore crystal structure (A$_2$B$_2$O$_7$ or A$_2$B$_2$O$_6$O', A and B are 3+ or 2+ and 4+ or 5+ cations) with $Fd\bar{3}m$ space group is typically described by using its similarity to simple fluorite structure (Fig. 7). In the ideal fluorite structure (MO$_2$, $Fm\bar{3}m$), the oxygen ions are located in the equivalent tetrahedral sites of an M face-centered cubic array. Similarly, in pyrochlores, two types of A and B cations form the face-centered cubic array exhibiting an

Fig. 6 Numbers of published items since 2002 covering the topics of TBCs and different material groups according to Web of Science^{TM}

alternating ABAB order at 16c and 16d sites in ⟨110⟩ directions, which result in doubling of the lattice parameter (*a*) with respect to the fluorite structure. However, due to this cation ordering in the pyrochlores, tetrahedral anion sites are no longer crystallographically identical; three distinct tetrahedral sites exist in the structure: the 48f, the 8a, and the 8b. Six oxygen atoms occupy the 48f sites with two A and two B neighbors, while the seventh oxygen occupies the 8b site surrounded by four A cations. The 8a site remains vacant; therefore, 87.5% of the tetrahedral sites are filled in the pyrochlore structure while in the ideal fluorite all of them are occupied (Ref 70).

The stability of the A3+, B4+ type pyrochlore structure (A is a lanthanide, and B is a transition metal) is governed by the ratio of the ionic radii of A and B cations (1.46 ≤ rA/rB ≤ 1.80). Accordingly, for instance, lanthanide zirconates (Ln: Gd → La) with the ionic radius ratio ranging from 1.46 to 1.61 adopt pyrochlore structure, while lanthanide zirconates (Ln: Lu→Tb) with the ionic radius ratio ranging from 1.35 to 1.44 crystallize in defect fluorite structure. The ordered pyrochlore structure can be transformed to defect fluorite structure by a random distribution of both cations and anions onto their individual sublattice, and such transformation can be induced by temperature, pressure, composition changes, or ion radiation (Ref 71). Effect of temperature and composition on the stability and relevant properties of lanthanide zirconates (Ln$_2$Zr$_2$O$_7$) for TBCs will be further discussed below.
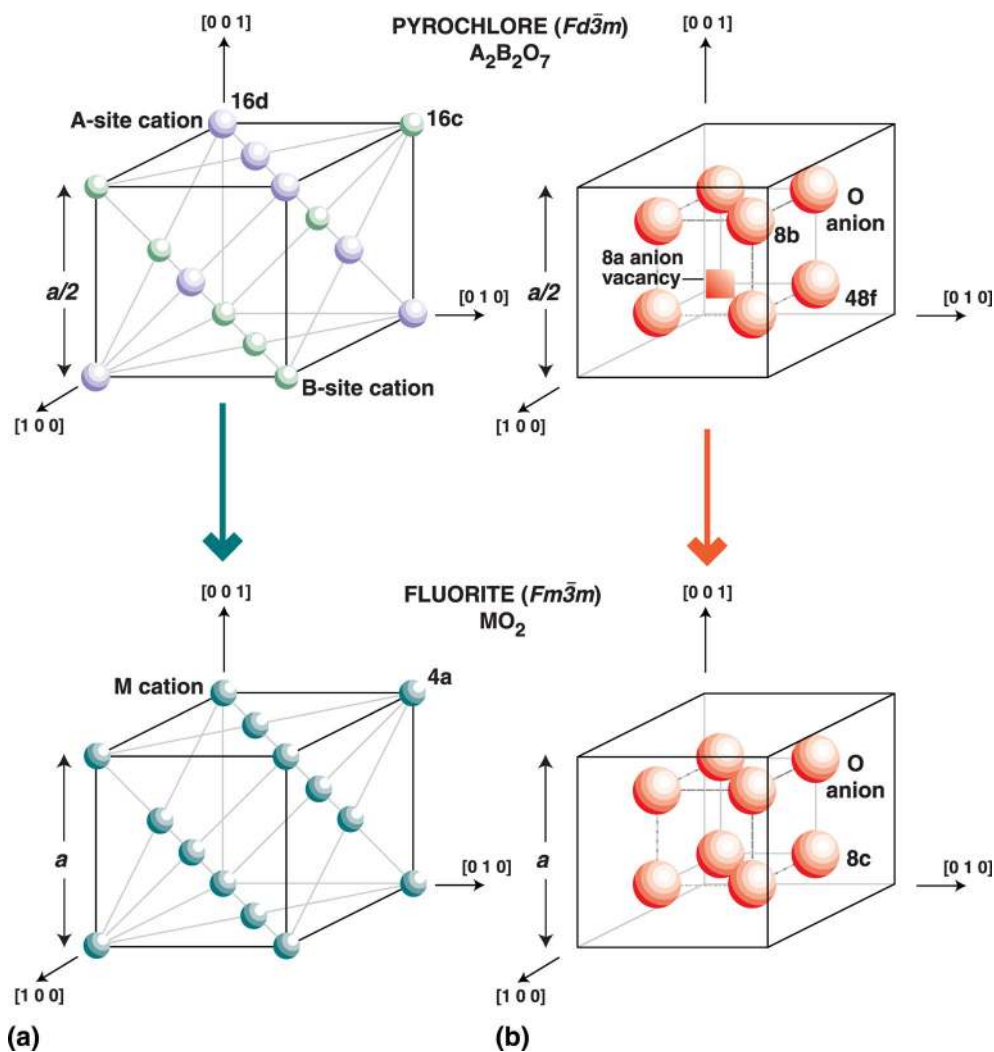
Thermal Conductivity

As a result of high concentration of intrinsic oxygen vacancies, high-level cation substitution (versus YSZ), and large atomic mass difference between zirconia and large lanthanides, which increases the phonon scattering strength of the point defects (Ref 72), Ln$_2$Zr$_2$O$_7$ (Ln: La, Nd, Sm, Eu, Gd) are attractive low thermal conductivity material candidates. Their thermal conductivities were reported between 1.2 and 2.2 W/mK in different studies (Table 2), although significant discrepancies are visible between the studies investigating the same material, which can be attributed to the different method of sintering and hence differences in the initial porosities of samples. Recently, Fabrichnaya et al. investigated the effect of sintering method on the measured thermal conductivities and demonstrated that the Ln$_2$Zr$_2$O$_7$ (Ln: La, Nd, Sm) samples sintered using the SPS/FAST (spark plasma sintering/field assisted sintering technique) have substantially higher thermal diffusivities and conductivities than that of the samples sintered conventionally at 1600 °C (Ref 73). A thermal conductivity of 2.2 W/mK for the SPS/FAST La$_2$Zr$_2$O$_7$ was reported in this study, which is quite similar to that of the YSZ.
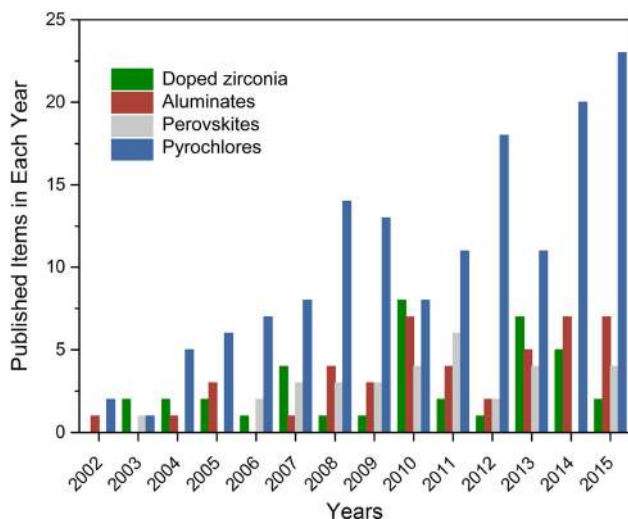
Fig. 7 Comparison of the cation (a) and anion (b) arrangements in the unit cells of pyrochlore ($A_2B_2O_7$) and fluorite (MO_2) compounds (Ref 116)

Further reductions in the thermal conductivity of the $Ln_2Zr_2O_7$ pyrochlores were achieved by cation dopings. Lehmann et al. showed that doping $La_2Zr_2O_7$ with 30% Nd (atomic mass, $m_a = 144.23$), Eu ($m_a = 151.94$) or Gd ($m_a = 157.25$) leads to a systematic reduction in the thermal conductivity with the increase in m_a of the doping element (Ref 74). Accordingly, a maximum reduction from 1.55 to 0.9 W/mK in the thermal conductivity was obtained with 30% Gd dopant at 800 °C. Bansal and Zhu also studied the thermal conductivity of the same material and revealed that doping $La_2Zr_2O_7$ with both Gd (15%) and Yb (15%) leads to additional reductions with respect to the solely Gd (30%)-doped $La_2Zr_2O_7$ (Ref 75). More recently, Guo et al. reported the thermal conductivities of Yb_2O_3 (Yb, $m_a = 173.05$)-doped $Gd_2Zr_2O_7$ ceramics as in a range of 0.88-1.00 W/mK at 1400 °C, about 20% lower than that of $Gd_2Zr_2O_7$ (1.2 W/mK) (Ref 76).

Although many experimental studies, especially on $Ln_2Zr_2O_7$ pyrochlores, are already available, measurements are typically limited to 800 °C. If they are not, then a pronounced contribution of radiative heat transfer at higher temperatures complicates the interpretation and understanding of point defects and phonon scattering at these high temperatures. In this regard, molecular dynamic (MD) simulations are shown to be useful for adapting and further developing earlier phonon models to get a better understanding of thermal transport in TBC materials. Schelling et al. investigated the effect of the size of A and B cations (A = La, Pr, Nd, Sm, Eu, Gd, Y, Er or Lu; B = Ti, Mo, Sn, Zr or Pb) on the thermal conductivity of forty different pyrochlore composition at 1200 °C and found a greater dependence on the B than A ionic radius (Ref 77). Furthermore, while results of different experimental studies indicate $Gd_2Zr_2O_7$ with the lowest thermal conductivity (1.2 W/mK)

Table 2 Properties of zirconate pyrochlores with large lanthanides ((La, Nd, Sm, Eu, Gd)Zr_2O_7) versus YSZ

Material	Thermal conductivity at 1000 °C, W/mK	Melting temperature/max. stability temperature of pyrochlore or YSZ, °C	CTE ($\times 10^{-6}$ K^{-1}) at 1000 °C
$La_2Zr_2O_7$	1.8 (Ref [118])	2283/2283 (L ↔ P) (Ref [119])	9.7 (Ref [120])
	1.6 (Ref [122])		9.2 (Ref [121])
	1.4 (Ref [97])		9.1 (Ref [74])
	2.1 (Ref [75])		
	2.2 (Ref [73])		
	1.5 (Ref [74])		
$Nd_2Zr_2O_7$	1.9 (Ref [123])	2320/2310 (F ↔ P) (Ref [119])	9.6 (Ref [74])
	1.3 (Ref [74])		
$Sm_2Zr_2O_7$	1.5 (Ref [124])	2497/2026 (F ↔ P) (Ref [119])	10.8 (Ref [125])
	1.8 (Ref [123])		
	1.3 (Ref [126])		
$Eu_2Zr_2O_7$	1.7 (Ref [124])	2475/1855 (F ↔ P) (Ref [127])	10.5 (Ref [74])
$Gd_2Zr_2O_7$	1.4 (Ref [118])	2570/1550 (F ↔ P) (Ref [119])	10.5 (Ref [74])
	1.5 (Ref [128])		11.5 (Ref [83])
	1.2 (Ref [97])		12.2 (Ref [76])
	1.2 (Ref [76])		
8 mol.% YSZ	2.1 (Ref [129])	2700/1200 (Ref [32])	10.1 (Ref [130])

L, *P*, and *F* denote liquid, pyrochlore, and fluorite phases, respectively

in $Ln_2Zr_2O_7$ group (Ln: La, Nd, Sm, Eu, Gd), the simulation results suggest no systematic dependence of thermal conductivity on the size of the A ion and predict $Nd_2Zr_2O_7$ as the most thermally insulating pyrochlore in this group. In the same study, some of the lanthanide-stannate pyrochlores and lanthanide-plumbate pyrochlores are predicted to have a lower thermal conductivity than lanthanide zirconates. However, Qu et al. (Ref [78]) measured the thermal conductivities of $Ln_2Sn_2O_7$ (Ln: La-Lu, Y) between 2.0 and 2.5 W/mK at 1000 °C and $Ln_2Pb_2O_7$ structures were reported to be unstable above 300 °C (Ref [70]).

High-Temperature Phase Stability

Another essential benefit of $Ln_2Zr_2O_7$ is their high-temperature phase stability. Unlike the YSZ, they remain as single phases over the entire service temperature range of the TBCs. Table 2 shows maximum stability temperatures of different $Ln_2Zr_2O_7$ (Ln: La, Nd, Sm, Eu, Gd) compositions as well as their melting temperatures. The former indicates the temperature at which pyrochlore (P) transforms to a so-called defect fluorite structure (F), as mentioned earlier. Accordingly, the $Gd_2Zr_2O_7$ has the lowest stability temperature in this group at about 1550 °C, and transformation temperature rises with increasing Ln cation size (Gd → Nb). In the La_2O_3-ZrO_2 system, the pyrochlore phase becomes stable all the way up to the liquidus

temperature (2283 °C) and thus no longer exhibits a solid state (F ↔ P) transition.

It should be mentioned here that when different pyrochlore compositions ($Ln_2Zr_2O_7$, Ln: La, Sm, Gd) were deposited on the substrates by plasma spraying, the as-sprayed coatings were found to be showing defect fluorite structure at room temperature (Ref [79-81]). This order-disorder transition is typically attributed to the high cooling rate of the molten particles in plasma spraying process, which could kinetically constrain the ordering process. Similarly, in EB-PVD process, as-deposited coatings were reported to be in defect fluorite phase, suggesting that even high substrate temperatures (1100 °C) cannot assist pyrochlore structure formation within the time scale of the deposition process (Ref [82]). After heat treatments or thermal cycling of the as-deposited coatings, defect fluorite was found to be ordered into pyrochlore structure. However, although no detrimental effect of this disorder-order transformation on the lifetime has been described, the degree of order in the as-deposited $Ln_2Zr_2O_7$ coatings, kinetics of disorder-order transformation and its possible effects on sintering rate of the coatings have not been reported.

Coefficient of Thermal Expansion

The CTEs of the dense pyrochlores ($Ln_2Zr_2O_7$, Ln: La, Nd, Sm, Eu, Gd) were reported between 9.1 and 12.2 $\times 10^{-6}$ K^{-1} at 1000 °C (Table 2). Although there are

significant differences between the results of different studies likely due to different measurement setups, it is clear that CTEs of the pyrochlores are close to that of the standard YSZ 11×10^{-6} K^{-1}.

In one of the early studies, two groups of zirconate pyrochlores: (1) Ln$_2$Zr$_2$O$_7$, Ln: La, Nd, Eu, Gd with systematically decreasing ion radius and (2) La$_2$Zr$_2$O$_7$ in which La is substituted with one of Nd, Eu and Gd (La$_{1.4}$(Nd)$_{0.6}$Zr$_2$O$_7$, La$_{1.4}$(Eu)$_{0.6}$Zr$_2$O$_7$, La$_{1.4}$(Gd)$_{0.6}$Zr$_2$O$_7$) were investigated (Ref [74]). For the first group, no simple dependence of CTE on the Ln cation size was found, except that La$_2$Zr$_2$O$_7$ which has the largest Ln cation in the group has the lowest CTE over the studied temperature range (RT-1400 °C). In the second group, CTE of partially substituted compounds was reported to be slightly different than the La$_2$Zr$_2$O$_7$ revealing that substitution of 30% La with other trivalent cations does not produce a sufficient distortion in the lattice leading to a significant change in CTEs. Another A-site doping investigation was made on Gd$_2$Zr$_2$O$_7$ by Guo et al. (Ref [76]). Yb was selected as a dopant element, which has the smallest ionic radii among rare-earth elements and hence reduces the value of r_A/r_B ratio in A$_2$B$_2$O$_7$, resulting in the stabilization of defect fluorite structure instead of the pyrochlore. The CTEs of the Yb$_2$O$_3$-doped Gd$_2$Zr$_2$O$_7$ ((Gd$_{1-x}$Yb$_x$)$_2$Zr$_2$O$_7$ ($x = 0$, 0.1, 0.3, 0.5, 0.7)) were found to be in the range of 11.8-13 $\times 10^{-6}$ K^{-1} at 1200 °C, which are comparable or even larger than that of the YSZ. Wan et al. investigated a B-site doping of Gd$_2$Zr$_2$O$_7$ and chose smaller Ti^{4+} to partially substitute Zr^{4+} (Ref [83]) based on the study of Hess et al. (Ref [84]), which suggest that the structural integrity of pyrochlore structure is mainly provided by the B-O bond pair. Therefore, weakening of Zr-O bonding may lead a structural relaxation and hence higher CTEs. The CTE of the Gd$_2$Zr$_2$O$_7$ was measured to be 11.5 $\times 10^{-6}$ K^{-1} at 1000 °C in this study which was increased to maximum 11.8 $\times 10^{-6}$ K^{-1} by Ti doping (Gd$_2$(Zr$_{1-x}$Ti$_x$)$_2$O$_7$, $x = 0.2$). A molecular dynamic simulation comparing the effect of A-site and B-site doping on the CTE of Sm$_2$Zr$_2$O$_7$ has been performed, and the results also showed a higher CTE for the latter (Sm$_2$(Ce$_{0.3}$Zr$_{0.7}$)O$_7$) than the former ((Gd$_{0.4}$Sm$_{0.5}$Yb$_{0.1}$)$_2$Zr$_2$O$_7$) (Ref [85]). Therefore, in the light of these findings, it can be speculated that the B-site doping in pyrochlore structure can be favorable for a higher CTE.

CMAS and Hot Corrosion Behavior

Superior CMAS resistance of Ln$_2$Zr$_2$O$_7$ with respect to the YSZ was presented in the last decade, which was a notable finding for the implementation of pyrochlores in TBCs (Ref [86, 87]). Initially, it was reported for an EB-PVD Gd$_2$Zr$_2$O$_7$ TBC that Gd$_2$Zr$_2$O$_7$ reacts with the CMAS melt resulting in the crystallization of a highly

stable apatite phase incorporating Ca, Gd, and Si at temperatures well above the melting point of the original deposit. This crystalline phase seals off the top of the coating and prevents further CMAS penetration as the reaction, and crystallization kinetics are competitive with that for the penetration (Ref [88]). Later on, the formation of a sealing layer made of Ca$_2$Gd$_8$(SiO$_4$)$_6$O$_2$ apatite phase was documented for an APS Gd$_2$Zr$_2$O$_7$ coating, as well (Fig. [8]). The CMAS penetration depth in the APS Gd$_2$Zr$_2$O$_7$ coating was noted as $\sim$20 μm after 24 h interaction at 1200 °C, while it was $\sim$200 μm for the APS YSZ coating under same test conditions. Moreover, infiltration resistance of APS Gd$_2$Zr$_2$O$_7$ against different type of molten silicate deposits (e.g., volcanic ash, coal fly ash) was reported in the same study.

Drexler et al. (Ref [89]) also compared the CMAS resistance of different rare-earth (Yb, Gd, Y) zirconate compositions, and a summary of their findings is given in Table [3]. Based on the results, more than a tenfold difference in the CMAS penetration depths of YSZ and Y$_2$Zr$_2$O$_7$ compositions clearly demonstrated that apatite phase formation and hence the CMAS mitigation resistance are controlled by Y^{3+} concentration in these compositions. Furthermore, different CMAS mitigation performances of the zirconia compositions containing a high concentration of Y$_2$O$_3$, Yb$_2$O$_3$, and Gd$_2$O$_3$ were observed and argued by different sizes of RE^{3+} as well as the formation of stoichiometrically different apatite phases with CMAS interaction. Authors' hypothesis was that, as more RE^{+3} cation incorporation is required to form the Gd apatite than the Y(or Yb) apatite, the CMAS melt needs to penetrate deeper to accumulate sufficient amount of RE^{+3} in Gd$_2$Zr$_2$O$_7$. On the other hand, although they form similar type of apatite phases, shorter penetration depth in Y$_2$Zr$_2$O$_7$ than Yb$_2$Zr$_2$O$_7$ was attributed to the larger size of Y^{3+} which results in a higher crystallization tendency of Y apatite.

More recently, Poerschke and Levi systematically investigated the relations between rare-earth oxide (RE: Yb, Gd, La) containing zirconia or hafnia-based compositions and their primary and secondary CMAS interaction products, such as the apatite, fluorite, and garnet (Ref [90]). Their results revealed that from the two most relevant reaction products to mitigate CMAS penetration, the apatite, and fluorite, the composition of former is relatively insensitive to the composition of the coating material in contrast to what Drexler et al. suggested. They found a strong correlation between the RE cation and the composition of fluorite phase instead. Furthermore, their result suggested that the effectiveness of crystallization reactions increases with larger RE cation sizes (Yb < Gd < La) in both zirconia- and hafnia-based systems. Supporting this finding, Schulz and Braue studied the CMAS infiltration response of La$_2$Zr$_2$O$_7$ and Gd$_2$Zr$_2$O$_7$ coatings deposited
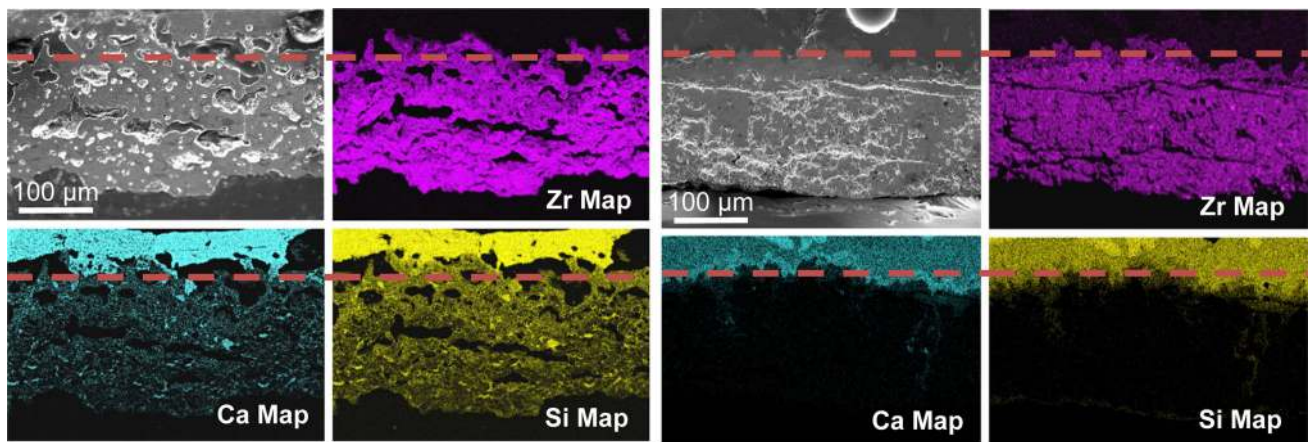
Fig. 8 Cross-sectional SEM micrograph of APS 7YSZ (left) and $Gd_2Zr_2O_7$ (right) TBCs and corresponding Zr, Ca, and Si elemental maps after interaction with CMAS glass (1200 °C, 24 h). The horizontal dashed line denotes top surface of the original TBC. Reproduced from Ref 117

Table 3 CMAS mitigation performance and reaction products of different rare-earth zirconates and 7YSZ after 24-h CMAS interaction at 1200 °C reported by Ref 89

Composition	Primary phases	Phases observed in the reaction zone after CMAS interaction	CMAS penetration depth, μm
$Y_2Zr_2O_7$ (37.5 mol.% Y_2O_3)	Cubic ZrO_2 solid solution	Y apatite, $Ca_4Y_6(SiO_4)_6O$	20 ± 3
$Gd_2Zr_2O_7$ (38.0 mol.% Gd_2O_3)	Fluorite	Gd apatite, $Ca_2Gd_8(SiO_4)_6O_2$	60 ± 4
$Yb_2Zr_2O_7$ (38.3 mol.% Yb_2O_3)	Cubic ZrO_2 solid solution + $Yb_4Zr_3O_{12}$	Yb apatite, $Ca_4Yb_6(SiO_4)_6O$	40 ± 3
7YSZ (3.9 mol.% Y_2O_3)	Tetragonal ZrO_2 solid solution	No apatite phase	263 ± 12

Note the different apatite phase stoichiometries of Y and Yb than Gd

with EB-PVD and found that the former reacts faster with the CMAS melt than the later (Ref 91). Additionally, their results revealed that the homogeneity of the columnar structure has a profound effect on the reaction kinetics and products as it alters the reaction interfaces and amount of CMAS supply to these reaction zones. Today it is better known that in addition to CMAS composition, viscosity, surface tension of the melts and test temperatures, TBC microstructure, particularly the microstructure of columnar structures, e.g., shape of the intercolumnar gaps, control the CMAS penetration depth of the same TBC material.

Hot corrosion behavior of pyrochlores has not been investigated as intensive as their CMAS resistance. Marple et al. (Ref 92) studied the hot corrosion of $La_2Zr_2O_7$ and YSZ coatings which were exposed to vanadium- and sulfur-containing compounds at temperatures up to 1000 °C. As mentioned earlier, the YSZ coatings are quite vulnerable to vanadium attacks, but they are relatively stable in the presence of sulfur-containing compounds. However, it was revealed with this study that, in contrast to the YSZ, the reaction of $La_2Zr_2O_7$ with V_2O_5 does not severely damage the coating, while the reactions with sulfur-containing compounds lead to the rapid degradation of the coating under the same test conditions. In another study, the superior hot corrosion resistance of $Gd_2Zr_2O_7$ coating than that of the YSZ under $Na_2SO_4 + V_2O_5$ attack at 1050 °C was reported (Ref 93). Different response of pyrochlores against these chemical attacks is evident with these studies compared to YSZ; however, defense mechanisms have not been well understood to this day.

Implementation Issues and Performance

In addition to their advantageous properties, some difficulties have been reported for the application of pyrochlores in TBCs. These issues and their effects on the performance of TBCs will be summarized below.

1. Thermochemical Compatibility with the Alumina TGO

Levi (Ref 94) demonstrated that when Y_2O_3, Gd_2O_3, and La_2O_3 are added to zirconia above their critical concentrations (Y_2O_3 ~20 mol.%, Gd_2O_3 ~34 mol.%, La_2O_3 ~5 mol.%), formation of garnet, perovskite and β alumina phases, respectively, is induced as a result of an interaction with alumina at 1200 °C. Bearing in mind that the $Ln_2Zr_2O_7$ phases are stabilized with ~33.3 mol.% Ln_2O_3 additions to zirconia, the implication was that all mentioned compositions are prone to degrade by diffusional interaction with Al_2O_3. Later on Leckie et al. (Ref 95) experimentally studied the interphase formation between the pre-oxidized sapphire substrates and EB-PVD $Gd_2Zr_2O_7$ coatings. They found that $Gd_2Zr_2O_7$ tends to react with alumina to form a porous $GdAlO_3$ perovskite interphase. A similar phenomenon was also observed between $Sm_2Zr_2O_7$ coatings and alumina in a later study (Ref 96). Therefore, starting with the early patents filed for the pyrochlore implementation in TBC systems, a YSZ interdiffusion barrier layer was suggested to achieve a better performance (Ref 97, 98). This also addresses the limited toughness of the pyrochlore materials.

2. Fracture Toughness

One of the foremost characteristics of plasma-sprayed 7-8 wt.% yttria-stabilized zirconia is high fracture toughness owing to its non-transformable tetragonal (t') phase. Although thermal conductivity of zirconia could be further reduced with increased yttria concentrations (e.g., 20 wt.% yttria addition), due to stabilization of cubic phase which exhibits higher brittleness, 7-8 wt.% yttria-stabilized zirconia has remained the material of choice for decades. Cubic pyrochlore oxides likewise suffer from a low intrinsic fracture toughness. Recently Dwivedi et al. (Ref 99) reported a two times higher fracture toughness of YSZ coating than the $Gd_2Zr_2O_7$ in the as-sprayed state. Thus, pyrochlores are coupled with a 7-8 wt.% YSZ interlayer close to the TGO as a workaround. Nevertheless, such adoption does not solve other issues related to toughness such as poor erosion resistance of pyrochlore coatings and still limits their lifetime. Therefore, increasing the fracture toughness of pyrochlores intrinsically is highly demanded and mainly two different approaches were followed in the literature to that end, doping the pyrochlore or reducing the RE_2O_3 content (Table 4). It should be noted that the toughness or indentation fracture resistance values that are given for each study in Table 4 were calculated using different equations as well as different sample preparation methods and, therefore, cannot be directly compared to each other, yet they give the extent of increase that could be achieved in each individual work.

Depending on the amount of RE_2O_3 content reduction, it resulted in the formation of either fluorite or pyrochlore phase and some improvements were observed in the indentation fracture resistance with decreasing RE_2O_3 contents (Ref 100-102). Schmitt et al. suggested that the decrease in the oxygen vacancy concentration with the reduced RE_2O_3 content might be playing a role in such fracture resistance enhancement (Ref 102). Furthermore, they reported significant improvements in the erosion durability of the fluorite phase EB-PVD coatings. Nevertheless, some increases are also expected in the thermal conductivity as well as CMAS penetration in these coatings due to lack of RE_2O_3 concentration.

Introducing secondary phases to improve the toughness of the cubic pyrochlore is a more complicated method as it typically brings the problem of phase incompatibility. In one of the earliest studies, the addition of TiO_2 into $GdO_{1.5}$-ZrO_2 was investigated and demonstrated that tetragonality (c/a ratio) of the structure and the toughness could be increased with additions of Ti^{4+} (Ref 103). However, the nature of toughening mechanism could not be elucidated as synthesized ternary compositions were no single phase (cubic, tetragonal, also monoclinic formation in the crack process zones). Furthermore, phase separation toward equilibrium phases was stated to be relatively rapid, hence diminishing the long-term stability of the investigated material system. Sc^{3+} was another small ion investigated to toughen $Gd_2Zr_2O_7$, and Wang et al. showed that with increasing Sc_2O_3 additions in the investigated range, fracture resistance can be improved (Ref 104). Authors indexed pyrochlore phase within the compositional parameter range of $x = 0$-0.1 and fluorite phase at $x = 0.2$ which also yielded the highest fracture resistance. Therefore, supporting Schmitt et al. (Ref 102), it is possible that ordering degree and oxygen vacancy concentration play a role in the toughness of $Gd_2Zr_2O_7$.

Li et al. reported an increase in the fracture resistance of $La_2Zr_2O_7$ from 1.6 to 2 Mpa $m^{1/2}$ with the additions of either 10 vol.% $BaTiO_3$ or nanosize YAG due to piezoelectric toughening of the former and different mechanisms such as grain boundary strengthening and grain size reduction in the latter (Ref 105, 106). But reactions between the matrix and the additions at high temperatures are still questionable in these systems because authors only show the phase composition of mixtures after sintering at 1450 °C (or at 1650 °C) for a few minutes.

Zhang et al. (Ref 107) investigated the addition of YSZ (8 wt.% Y_2O_3) into $Gd_2Zr_2O_7$ (also into a number of different material groups) and showed increasing fracture resistance with increasing YSZ concentrations. The enhancement was attributed to crack deflection due to thermal expansion mismatches and stronger interfacial bonding between the

Table 4 A summary of toughness improvement studies for the pyrochlores

Toughening agent	Pyrochlore composition	Investigated stoichiometry	Indentation toughness, J/m² or indentation fracture resistance, MPa m$^{1/2}$		References
			Pyrochlore	Max. achieved after modification	
Effect of non-stoichiometry	$Nd_2Zr_2O_7$	$Nd_{2-x}Zr_{2+x}O_{7+x/2}$ ($x = 0.1, 0.2, 0.3, 0.4, 0.5$)	1.3 MPa m$^{1/2}$	2.5 MPa m$^{1/2}$ ($x = 0.5$)	Ref 100
Effect of non-stoichiometry	$Gd_2Zr_2O_7$	$Gd_{2-x}Zr_{2+x}O_{7+x/2}$ ($x = 0.1, 0.3, 0.5, 0.7$)	1.25 MPa m$^{1/2}$	2.25 MPa m$^{1/2}$ ($x = 0.7$)	Ref 101
Effect of sub-stoichiometry	$Gd_2Zr_2O_7$	$x(GdO_{1.5}).(1 - x)ZrO_2$ ($x = 15.66, 31.58, 41.88$ mol.%)	1.03 MPa m$^{1/2}$	1.25 MPa m$^{1/2}$ ($x = 15.66$ mol.%)	Ref 102
TiO_2	$Gd_2Zr_2O_7$	$xGdO_{1.5}/yTiO_2$-stabilized zirconia ($x = 7.6, 15$ mol.%) ($y = 0, 7, 15$ mol.%)	15 J/m²	60 J/m² ($x = 15$, $y = 15$ mol.%)	Ref 103
Sc_2O_3	$Gd_2Zr_2O_7$	$(Gd_{1-x}Sc_x)_2Zr_2O_7$ ($x = 0.025, 0.05, 0.075, 0.1, 0.2$)	0.8 MPa m$^{1/2}$	1.5 MPa m$^{1/2}$ ($x = 0.2$)	Ref 104
$Y_3Al_5O_{12}$ (YAG)	$La_2Zr_2O_7$	$xYAG/(1 - x)La_2Zr_2O_7$ ($x = 10, 15, 20$ vol.%)	1.6 MPa m$^{1/2}$	2 MPa m$^{1/2}$ ($x = 10$ vol.%)	Ref 105
$BaTiO_3$	$La_2Zr_2O_7$	$xBaTiO_3/(1 - x)La_2Zr_2O_7$ ($x = 5, 10, 15, 20$ vol.%)	1.6 MPa m$^{1/2}$	2 MPa m$^{1/2}$ ($x = 10$ vol.%)	Ref 106
YSZ (8 wt. Y_2O_3%)	$Gd_2Zr_2O_7$	$xYSZ /(1 - x) Gd_2Zr_2O_7$ ($x = 20, 50, 80$ wt.%)	0.75 MPa m$^{1/2}$	3 MPa m$^{1/2}$ ($x = 80$ wt.%)	Ref 107
YSZ (3 mol. Y_2O_3%)	$Gd_2Zr_2O_7$	$xYSZ /(1 - x) Gd_2Zr_2O_7$ ($x = 10, 20, 30,..., 80$ vol.%)	1.2 MPa m$^{1/2}$	2 MPa m$^{1/2}$ ($x = 80$ vol.%)	Ref 108
YbSZ (3.5 mol. Yb_2O_3%)	$Gd_2Zr_2O_7$	$xYbSZ /(1 - x) Gd_2Zr_2O_7$ ($x = 5, 10, 15, 20, 40$ mol.%)	1.3 MPa m$^{1/2}$	1.9 MPa m$^{1/2}$ ($x = 40$ mol.%)	Ref 109
ErSZ (3.5 mol. Er_2O_3%)	$Gd_2Zr_2O_7$	$xErSZ/(1 - x) Gd_2Zr_2O_7$ ($x = 10, 15, 20, 40$ mol.%)	0.85 MPa m$^{1/2}$	1.25 MPa m$^{1/2}$ ($x = 40$ mol.%)	Ref 110
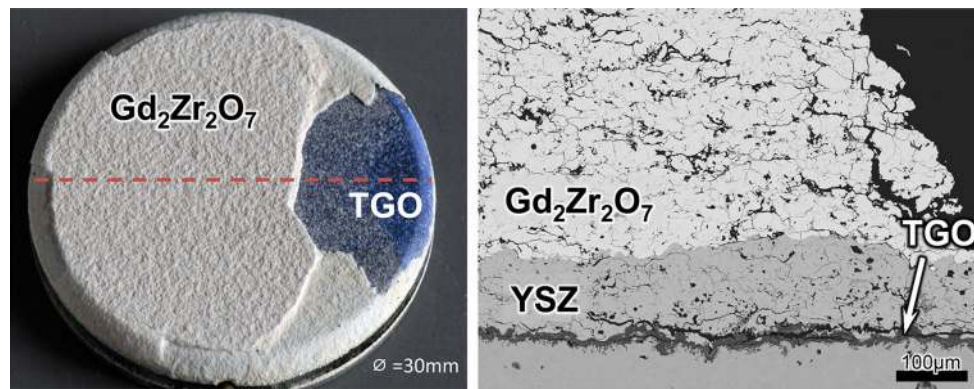
Fig. 9 Photograph (left) and cross-sectional microstructure (right) showing the failure mode of thermally cycled $Gd_2Zr_2O_7$/YSZ TBC system in burner rig setup. Dashed line on the photograph indicates the cutting plane for metallographic sample preparation. The test was conducted at 1394/1066 °C surface/bond coat temperature gradient and sample failed after 2055 cycles

secondary phases; however, this explanation cannot describe the toughening in the single fluorite phase YSZ-$Gd_2Zr_2O_7$ solutions that were reported in this study. Ma et al. (Ref 108) also introduced YSZ (3 mol.% Y_2O_3, nanosize) and showed increasing trend in the fracture resistance of $Gd_2Zr_2O_7$ at higher YSZ concentrations. Their result revealed that up to 80 vol.% addition of 3YSZ, a fluorite phase stabilizes and at higher concentrations phase partitioning occurs in the supersaturated solid solution. Therefore, it is clear from both studies working on the YSZ that the fluorite phase formation results in higher toughness over pyrochlore but the mechanism is uncertain.

To take advantage of ferroelastic toughening mechanism of t' phase, doping of $Gd_2Zr_2O_7$ with Er_2O_3-stabilized zirconia (ErSZ) and Yb_2O_3-stabilized zirconia (YbSZ) was studied by another group (Ref 109, 110). It was shown in these studies that the t' phase stability of YbSZ and ErSZ at 1400 °C is relatively better than that of YSZ. After 100-h annealing at 1400 °C, the monoclinic and cubic phase content in the YbSZ was reported to be 4.8 and 19.9 mol.% (rest is tetragonal), respectively, while according to study of Miller et al. (Ref 32) tetragonal content in the YSZ (8.6 wt.% Y_2O_3) was reduced to 30% at the same annealing conditions. Their results suggested that between 15-40 mol.% ErSZ or YbSZ addition into $Gd_2Zr_2O_7$ a t' phase stabilizes and leads to an increase in the fracture resistance.

An overarching conclusion is that, although there were several attempts to increase the toughness of the pyrochlores, the obtained improvements, if any, are published only based on indentation test results and seem to be at the expense of the CMAS resistance or the low thermal conductivity of the investigated materials.

3. Processability and Performance

Vaßen et al. (Ref 61) compared the thermal cycling lifetime of the APS $Ln_2Zr_2O_7$ (Ln: La, Gd), APS YSZ, and double-layer APS YSZ/ $Ln_2Zr_2O_7$ (Ln: La, Gd) TBC systems under a temperature gradient (1300-1400 °C surface and 1070-1090 °C bond coat temperatures). At this high surface temperatures, the lifetime of the double layers was found to be superior to single layer YSZ and $Ln_2Zr_2O_7$ (Ln: La, Gd) systems, revealing that a surface temperature increase of at least 100 K compared to standard YSZ (1200 °C) possible with the use of $Ln_2Zr_2O_7$, if $Ln_2Zr_2O_7$ are combined with the YSZ interlayer. Later on, the potential of double-layer approach was established by several studies using different $Ln_2Zr_2O_7$ compositions or different processing techniques (EB-PVD, SPS, PS-PVD) (Ref 27, 29, 64, 80, 96). As an example, Fig. 9 shows the photograph and microstructure of an APS $Gd_2Zr_2O_7$/YSZ double-layer TBC after thermal cycling, which exhibits a typical TGO growth driven failure after 2055 cycles. At the very similar thermal cycling conditions, lifetime of the standard YSZ is in the range of 1000 cycles which clearly reveals the achieved improvement with this double-layer system.

For more than a decade, it has been also known that difference in the vapor pressures of Ln_2O_3 and zirconia complicates the processing of $Ln_2Zr_2O_7$ with both APS and EB-PVD processes. However, the Ln_2O_3 with higher vapor pressure than zirconia is prone to evaporate at high process temperatures resulting in as-deposited coatings containing metastable zirconia, which transform and then undergo specific volume changes during thermal cycling. There is a paucity of information on the thermodynamic properties of these solid solutions in the literature; however, based on the report of Jacobson it can be generalized that the differences between the vapor pressures of zirconia and Ln_2O_3 increase with decreasing atomic mass of the lanthanide elements (Ref 111). Obviously, the intermolecular bonds get stronger when the atomic mass increases so that it is more difficult to break those bonds to escape as a gaseous phase. Given that the La has smallest atomic mass in the lanthanide series, $La_2Zr_2O_7$ can be expected to be the most problematic pyrochlore composition to deposit, which

was stated in a number of APS and EB-PVD studies (Ref 62, 79, 112, 113). In the meantime, only minor compositional changes have been reported for $Sm_2Zr_2O_7$ and $Gd_2Zr_2O_7$ coatings (Ref 82, 114).

Cao et al. (Ref 112) addressed that thermal cycling performance of $La_2Zr_2O_7$ coatings is affected by the fast La_2O_3 loss during the plasma spraying process, and this can be prevented to some extent by increasing the amount of La_2O_3 in the feedstock. However, due to the fact that the evaporation rate of the sprayed powder is also influenced by the particle size, e.g., vaporization from a small particle will occur sooner than a larger particle, it is not possible to entirely control the homogeneity of the coating composition by this way. Hence, a more sophisticated material-related solution is needed in this regard. Mauer et al. reported that burner rig lifetime of a La_2O_3-depleted $La_2Zr_2O_7$ coating can be as short as 14 cycles at 1400 °C surface temperature and demonstrated that particle diagnostics can be a useful tool for tuning the particle temperatures during plasma spraying to have the least evaporation (Ref 79). Likewise, Xu et al. (Ref 113) showed that the thermal cycling lifetime of EB-PVD $La_2Zr_2O_7$ coatings is affected by non-stoichiometry in the coatings, which can be improved by properly controlling the electron beam current or by changing the ingot composition.

Summary

In this study, research activities on the developments of TBC ceramic top coats are reviewed. Established and developing thermal spray methods, properties of the state-of-the-art YSZ, as well as emerging ceramic materials, were discussed. The recent TBC literature clearly reveals the potential of lanthanide-zirconate-pyrochlores for further increasing the TBC service temperatures as well as for CMAS protection, while the newer processing technologies are combining high strain tolerance in the top coats with good cost-efficiency. Nevertheless, use of a double-layer TBC structures including a YSZ layer seems to be a prerequisite for taking advantage of the new materials. Furthermore, deposition of the new materials is proven to be more troublesome than the standard YSZ, meaning much more efforts required to achieve reliable and reproducible processing.

References

1. Forecast International Predicts a World Market for 5480 Industrial Power Generating Gas Turbine Engines Worth $105 Billion over the Next 10 Years, https://www.forecastinternational.com/press/release.cfm?article=13562. Accessed 15 Feb 2017

2. Forecast International: 15-Year World Aviation Gas Turbine Market Worth a Staggering $1.2 Trillion, https://www.forecastinternational.com/press/release.cfm?article=13551. Accessed 15 Feb 2017

3. S. Stecura, Two-Layer Thermal Barrier Coating for High Temperature Components, *Am. Ceram. Soc. Bull.*, 1978, **56**(12), p 1082-1085

4. D.P.H. Hasselman, L.F. Johnson, L.D. Bentsen, S. Rahmatullah, L.L. Hong, and M.V. Swain, Thermal Diffusivity and Conductivity of Dense Polycrystalline ZrO_2 Ceramics: A Survey, *Am. Ceram. Soc. Bull.*, 1987, **66**, p 799-806

5. L. Pawlowski, D. Lombard, and P. Fauchais, Structure-Thermal Properties-Relationship in Plasma Sprayed Zirconia Coatings, *J. Vac. Sci. Technol. A*, 1985, **3**(6), p 2494-2500

6. X.Q. Cao, R. Vassen, and D. Stoever, Ceramic Materials for Thermal Barrier Coatings, *J. Eur. Ceram. Soc.*, 2004, **24**(1), p 1-10

7. U. Schulz, B. Saruhan, K. Fritscher, and C. Leyens, Review on Advanced EB-PVD Ceramic Topcoats for TBC Applications, *Int. J. Appl. Ceram. Technol.*, 2004, **1**(4), p 302-315

8. N.P. Padture, M. Gell, and E.H. Jordan, Thermal Barrier Coatings for Gas-Turbine Engine Applications, *Science*, 2002, **296**(5566), p 280-284

9. L. Pawlowski, *The Science and Engineering of Thermal Spray Coatings*, Wiley, London, 2008

10. S. Kuroda and T.W. Clyne, The Quenching Stress in Thermally Sprayed Coatings, *Thin Solid Films*, 1991, **200**(1), p 49-66

11. M. Ahrens, R. Vaßen, D. Stöver, and S. Lampenscherf, Sintering and Creep Processes in Plasma-Sprayed Thermal Barrier Coatings, *J. Therm. Spray Technol.*, 2004, **13**(3), p 432-442

12. G. Gualco, S. Corcoruto, A. Campora, R. Taylor, D. Schwingel, and S. Oswald, Highly porous thick thermal barrier coatings produced by air plasma spraying of a plastic-ceramic mixed powder, *Therm. Spray United Forum Sci. Technol. Adv.*, 1997, **9**, p 305-313

13. W. Gao, *Developments in High Temperature Corrosion and Protection of Materials*, Elsevier Science, Amsterdam, 2008

14. G.P. Cherepanov, R. De Witt, and W. Cooley, *Mechanics of brittle fracture*, McGraw-Hill International Book Co., New York, 1979

15. T.A. Taylor, Thermal Properties and Microstructure of Two Thermal Barrier Coatings, *Surf. Coat. Technol.*, 1992, **54**, p 53-57

16. T.A. Taylor, D.L. Appleby, A.E. Weatherill, and J. Griffiths, Plasma-Sprayed Yttria-Stabilized Zirconia Coatings: Structure-Property Relationships, *Surf. Coat. Technol.*, 1990, **43-44**, p 470-480

17. H.B. Guo, R. Vaßen, and D. Stöver, Atmospheric Plasma Sprayed Thick Thermal Barrier Coatings with High Segmentation Crack Density, *Surf. Coat. Technol.*, 2004, **186**(3), p 353-363

18. M. Peters, K. Fritscher, G. Staniek, W.A. Kaysser, and U. Schulz, Design and Properties of Thermal Barrier Coatings for Advanced Turbine Engines, *Materialwiss. Werkstofftech.*, 1997, **28**(8), p 357-362

19. P. Fauchais, R. Etchart-Salas, V. Rat, J.F. Coudert, N. Caron, and K. Wittmann-Ténèze, Parameters Controlling Liquid Plasma Spraying: Solutions, Sols, or Suspensions, *J. Therm. Spray Technol.*, 2008, **17**(1), p 31-59

20. E.H. Jordan, C. Jiang, J. Roth, and M. Gell, Low Thermal Conductivity Yttria-Stabilized Zirconia Thermal Barrier Coatings Using the Solution Precursor Plasma Spray Process, *J. Therm. Spray Technol.*, 2014, **23**(5), p 849-859

21. H. Kassner, R. Siegert, D. Hathiramani, R. Vassen, and D. Stoever, Application of Suspension Plasma Spraying (SPS) for Manufacture of Ceramic Coatings, *J. Therm. Spray Technol.*, 2008, **17**(1), p 115-123

22. A. Guignard, G. Mauer, R. Vaßen, and D. Stöver, Deposition and Characteristics of Submicrometer-Structured Thermal Barrier Coatings by Suspension Plasma Spraying, *J. Therm. Spray Technol.*, 2012, **21**(3), p 416-424

23. L. Pawlowski, Suspension and Solution Thermal Spray Coatings, *Surf. Coat. Technol.*, 2009, **203**(19), p 2807-2829

24. N. Curry, K. VanEvery, T. Snyder, and N. Markocsan, Thermal Conductivity Analysis and Lifetime Testing of Suspension Plasma-Sprayed Thermal Barrier Coatings, *Coatings*, 2014, **4**(3), p 630

25. K. VanEvery, M.J.M. Krane, R.W. Trice, H. Wang, W. Porter, M. Besser, D. Sordelet, J. Ilavsky, and J. Almer, Column Formation in Suspension Plasma-Sprayed Coatings and Resultant Thermal Properties, *J. Therm. Spray Technol.*, 2011, **20**(4), p 817-828

26. M. Karger, R. Vaßen, and D. Stöver, Atmospheric Plasma Sprayed Thermal Barrier Coatings with High Segmentation Crack Densities: Spraying Process, Microstructure and Thermal Cycling Behavior, *Surf. Coat. Technol.*, 2011, **206**(1), p 16-23

27. S. Mahade, N. Curry, S. Björklund, N. Markocsan, P. Nylén, and R. Vaßen, Functional Performance of $Gd_2Zr_2O_7$/YSZ Multi-layered Thermal Barrier Coatings Deposited by Suspension Plasma Spray, *Surf. Coat. Technol.*, 2017, **318**, p 208-216 (Corrected proof)

28. K.V. Niessen, M. Gindrat, and A. Refke, Vapor Phase Deposition Using Plasma Spray-PVD, *J. Therm. Spray Technol.*, 2010, **19**(1-2), p 502-509

29. S. Rezanka, G. Mauer, and R. Vaßen, Improved Thermal Cycling Durability of Thermal Barrier Coatings Manufactured by PS-PVD, *J. Therm. Spray Technol.*, 2014, **23**(1-2), p 182-189

30. J.A. Thompson and T.W. Clyne, The Effect of Heat Treatment on the Stiffness of Zirconia Top Coats in Plasma-Sprayed TBCs, *Acta Mater.*, 2001, **49**(9), p 1565-1575

31. J.A. Krogstad, S. Krämer, D.M. Lipkin, C.A. Johnson, D.R.G. Mitchell, J.M. Cairney, and C.G. Levi, Phase Stability of t′-Zirconia-Based Thermal Barrier Coatings: Mechanistic Insights, *J. Am. Ceram. Soc.*, 2011, **94**, p s168-s177

32. J.L.S.R.A. Miller and R.G. Garlick, *Phase Stability in Plasma-Sprayed Partially Stabilized Zirconia-Yttria*, The American Ceramic Society, Columbus, 1981

33. A.V. Virkar and R.L.K. Matsumoto, Ferroelastic Domain Switching as a Toughening Mechanism in Tetragonal Zirconia, *J. Am. Ceram. Soc.*, 1986, **69**(10), p C-224-C-226

34. C. Mercer, J.R. Williams, D.R. Clarke, and A.G. Evans, On a Ferroelastic Mechanism Governing the Toughness of Metastable Tetragonal-Prime Yttria-Stabilized Zirconia, *Proc. R. Soc. Lond. A Math. Phys. Eng. Sci.*, 2007, **463**(2081), p 1393-1408

35. J. Chevalier, L. Gremillard, A.V. Virkar, and D.R. Clarke, The Tetragonal-Monoclinic Transformation in Zirconia: Lessons Learned and Future Trends, *J. Am. Ceram. Soc.*, 2009, **92**(9), p 1901-1920

36. J.R. Brandon and R. Taylor, Phase Stability of Zirconia-Based Thermal Barrier Coatings Part II. Zirconia-Ceria Alloys, *Surf. Coat. Technol.*, 1991, **46**(1), p 91-101

37. R.L. Jones and D. Mess, Improved Tetragonal Phase Stability at 1400 °C with Scandia, Yttria-Stabilized Zirconia, *Surf. Coat. Technol.*, 1996, **86**, p 94-101

38. T.A. Schaedler, R.M. Leckie, S. Krämer, A.G. Evans, and C.G. Levi, Toughening of Nontransformable t′-YSZ by Addition of Titania, *J. Am. Ceram. Soc.*, 2007, **90**(12), p 3896-3901

39. F.M. Pitek and C.G. Levi, Opportunities for TBCs in the ZrO_2-YO1.5-TaO2.5 System, *Surf. Coat. Technol.*, 2007, **201**(12), p 6044-6050

40. A.M. Limarga, S. Shian, R.M. Leckie, C.G. Levi, and D.R. Clarke, Thermal Conductivity of Single- and Multi-phase Compositions in the ZrO_2-Y_2O_3-Ta_2O_5 System, *J. Eur. Ceram. Soc.*, 2014, **34**(12), p 3085-3094

41. O. Fabrichnaya and F. Aldinger, Assessment of Thermodynamic Parameters in the System ZrO_2-Y_2O_3-Al_2O_3, *Zeitschrift für Metallkunde*, 2004, **95**(1), p 27-39

42. S.M. Lakiza and L.M. Lopato, Stable and Metastable Phase Relations in the System Alumina–Zirconia–Yttria, *J. Am. Ceram. Soc.*, 1997, **80**(4), p 893-902

43. J.R. Nicholls, M.J. Deakin, and D.S. Rickerby, A Comparison Between the Erosion Behaviour of Thermal Spray and Electron Beam Physical Vapour Deposition Thermal Barrier Coatings, *Wear*, 1999, **233-235**, p 352-361

44. R.L. Jones, Some Aspects of the Hot Corrosion of Thermal Barrier Coatings, *J. Therm. Spray Technol.*, 1997, **6**(1), p 77-84

45. R.L. Jones, R.F. Reidy, and D. Mess, Scandia, Yttria-Stabilized Zirconia for Thermal Barrier Coatings, *Surf. Coat. Technol.*, 1996, **82**(1-2), p 70-76

46. F.H. Stott, D.J. de Wet, and R. Taylor, Degradation of Thermal-Barrier Coatings at Very High Temperatures, *MRS Bull.*, 1994, **19**, p 46-49

47. C. Mercer, S. Faulhaber, A.G. Evans, and R. Darolia, A Delamination Mechanism for Thermal Barrier Coatings Subject to Calcium–Magnesium–Alumino–Silicate (CMAS) Infiltration, *Acta Mater.*, 2005, **53**(4), p 1029-1039

48. S. Krämer, J. Yang, C.G. Levi, and C.A. Johnson, Thermochemical Interaction of Thermal Barrier Coatings with Molten CaO-MgO-Al_2O_3-SiO_2 (CMAS) Deposits, *J. Am. Ceram. Soc.*, 2006, **89**(10), p 3167-3175

49. A. Aygun, A.L. Vasiliev, N.P. Padture, and X. Ma, Novel Thermal Barrier Coatings that are Resistant to High-Temperature Attack by Glassy Deposits, *Acta Mater.*, 2007, **55**(20), p 6734-6745

50. W. Li, H. Zhao, X. Zhong, L. Wang, and S. Tao, Air Plasma-Sprayed Yttria and Yttria-Stabilized Zirconia Thermal Barrier Coatings Subjected to Calcium–Magnesium–Alumino–Silicate (CMAS), *J. Therm. Spray Technol.*, 2014, **23**(6), p 975-983

51. P. Ramaswamy, S. Seetharamu, K.J. Rao, and K.B.R. Varma, Thermal Shock Characteristics of Plasma Sprayed Mullite Coatings, *J. Therm. Spray Technol.*, 1998, **7**(4), p 497-504

52. N.P. Padture and P.G. Klemens, Low Thermal Conductivity in Garnets, *J. Am. Ceram. Soc.*, 1997, **80**(4), p 1018-1020

53. X. Zhou, Z. Xu, X. Fan, S. Zhao, X. Cao, and L. He, $Y_4Al_2O_9$ Ceramics as a Novel Thermal Barrier Coating Material for High-Temperature Applications, *Mater. Lett.*, 2014, **134**, p 146-148

54. D.A. Hirschfeld, D.M. Liu, and J.J. Brown, CMZP-a new high temperature thermal barrier material, in *The 4th International Symposium on Ceramic Materials and Components for Engines*, ed. by R. Carlsson, R. Johansson, and L. Kahlman (Elsevier Applied Science, London, 1992), pp. 370-372

55. D. Zhu and R.A. Miller, Development of Advanced Low Conductivity Thermal Barrier Coatings, *Int. J. Appl. Ceram. Technol.*, 2004, **1**(1), p 86-94

56. D. Zhu, J.A. Nesbitt, C.A. Barrett, T.R. McCue, and R.A. Miller, Furnace Cyclic Oxidation Behavior of Multicomponent Low Conductivity Thermal Barrier Coatings, *J. Therm. Spray Technol.*, 2004, **13**(1), p 84-92

57. W. Ma, M.O. Jarligo, D.E. Mack, D. Pitzer, J. Malzbender, R. Vaßen, and D. Stöver, New Generation Perovskite Thermal Barrier Coating Materials, *J. Therm. Spray Technol.*, 2008, **17**(5-6), p 831-837

58. M.O. Jarligo, G. Mauer, D. Sebold, D.E. Mack, R. Vaßen, and D. Stöver, Decomposition of $Ba(Mg_{1/3}Ta_{2/3})O_3$ Perovskite During Atmospheric Plasma Spraying, *Surf. Coat. Technol.*, 2012, **206**(8-9), p 2515-2520

59. M.O. Jarligo, D.E. Mack, R. Vassen, and D. Stöver, Application of Plasma-Sprayed Complex Perovskites as Thermal Barrier Coatings, *J. Therm. Spray Technol.*, 2009, **18**(2), p 187-193

60. W. Ma, D. Mack, J. Malzbender, R. Vaßen, and D. Stöver, Yb$_2$O$_3$ and Gd$_2$O$_3$ Doped Strontium Zirconate for Thermal Barrier Coatings, *J. Eur. Ceram. Soc.*, 2008, **28**(16), p 3071-3081

61. R. Vaßen, F. Träger, and D. Stöver, New Thermal Barrier Coatings Based on Pyrochlore/YSZ Double-Layer Systems, *Int. J. Appl. Ceram. Technol.*, 2004, **1**(4), p 351-361

62. B. Saruhan, P. Francois, K. Fritscher, and U. Schulz, EB-PVD Processing of Pyrochlore-Structured La$_2$Zr$_2$O$_7$-Based TBCs, *Surf. Coat. Technol.*, 2004, **182**(2-3), p 175-183

63. X.Q. Cao, R. Vassen, F. Tietz, and D. Stoever, New Double-Ceramic-Layer Thermal Barrier Coatings Based on Zirconia–Rare Earth Composite Oxides, *J. Eur. Ceram. Soc.*, 2006, **26**(3), p 247-251

64. Z. Xu, L. He, R. Mu, X. Zhong, Y. Zhang, J. Zhang, and X. Cao, Double-Ceramic-Layer Thermal Barrier Coatings Of La$_2$Zr$_2$O$_7$/YSZ Deposited by Electron Beam-Physical Vapor Deposition, *J. Alloys Compd.*, 2009, **473**(1-2), p 509-515

65. M.K. Cinibulk, Thermal Stability of Some Hexaluminates at 1400 °C, *J. Mater. Sci. Lett.*, 1995, **14**(9), p 651-654

66. R. Gadow and M. Lischka, Lanthanum Hexaaluminate—Novel Thermal Barrier Coatings for Gas Turbine Applications—Materials and Process Development, *Surf. Coat. Technol.*, 2002, **151-152**, p 392-399

67. G.W. Schäfer and R. Gadow, Lanthanum Aluminate Thermal Barrier Coating, *Ceram. Eng. Sci. Proc.*, 1999, **20**(4), p 291-297

68. X.Q. Cao, Y.F. Zhang, J.F. Zhang, X.H. Zhong, Y. Wang, H.M. Ma, Z.H. Xu, L.M. He, and F. Lu, Failure of the Plasma-Sprayed Coating of Lanthanum Hexaluminate, *J. Eur. Ceram. Soc.*, 2008, **28**(10), p 1979-1986

69. X. Xie, H. Guo, S. Gong, and H. Xu, Lanthanum–Titanium–Aluminum Oxide: A Novel Thermal Barrier Coating Material for Applications at 1300 °C, *J. Eur. Ceram. Soc.*, 2011, **31**(9), p 1677-1683

70. M.A. Subramanian, G. Aravamudan, and G.V. Subba Rao, Oxide Pyrohlores-A Review, *Prog. Solid State Chem.*, 1983, **15**, p 55-143

71. F.X. Zhang, M. Lang, and R.C. Ewing, Atomic Disorder in Gd$_2$Zr$_2$O$_7$ Pyrochlore, *Appl. Phys. Lett.*, 2015, **106**(19), p 191902

72. J. Wu, N.P. Padture, P.G. Klemens, M. Gell, E. Garcia, P. Miranzo, and M.I. Osendi, Thermal Conductivity of Ceramics in the ZrO$_2$-GdO$_{1.5}$ System, *J. Mater. Res.*, 2002, **17**(12), p 3193-3200

73. O. Fabrichnaya, R. Wulf, M.J. Kriegel, G. Savinykh, M. Dopita, J. Seidel, H.C. Heitz, O. Nashed, U. Gross, and H.J. Seifert, Thermophysical Properties of Pyrochlore and Fluorite Phases in the Ln$_2$Zr$_2$O$_7$-Y$_2$O$_3$ Systems (Ln = La, Nd, Sm): 1. Pure Pyrochlores and Phases in the La$_2$Zr$_2$O$_7$-Y$_2$O$_3$ System, *J. Alloys Compd.*, 2014, **586**, p 118-128

74. H. Lehmann, D. Pitzer, G. Pracht, R. Vassen, and D. Stöver, Thermal Conductivity and Thermal Expansion Coefficients of the Lanthanum Rare-Earth-Element Zirconate System, *J. Am. Ceram. Soc.*, 2003, **86**(8), p 1338-1344

75. N.P. Bansal and D. Zhu, Effects of Doping on Thermal Conductivity of Pyrochlore Oxides for Advanced Thermal Barrier Coatings, *Mater. Sci. Eng. A*, 2007, **459**(1-2), p 192-195

76. L. Guo, H. Guo, H. Peng, and S. Gong, Thermophysical Properties of Yb$_2$O$_3$ Doped Gd$_2$Zr$_2$O$_7$ and Thermal Cycling Durability of (Gd$_{0.9}$Yb$_{0.1}$)$_2$Zr$_2$O$_7$/YSZ Thermal Barrier Coatings, *J. Eur. Ceram. Soc.*, 2014, **34**(5), p 1255-1263

77. P.K. Schelling, S.R. Phillpot, and R.W. Grimes, Optimum Pyrochlore Compositions for Low Thermal Conductivity, *Philos. Mag. Lett.*, 2004, **84**(2), p 127-137

78. Z. Qu, C. Wan, and W. Pan, Thermophysical Properties of Rare-Earth Stannates: Effect of Pyrochlore Structure, *Acta Mater.*, 2012, **60**(6-7), p 2939-2949

79. G. Mauer, D. Sebold, R. Vaßen, and D. Stöver, Improving Atmospheric Plasma Spraying of Zirconate Thermal Barrier Coatings Based on Particle Diagnostics, *J. Therm. Spray Technol.*, 2012, **21**(3-4), p 363-371

80. E. Bakan, D.E. Mack, G. Mauer, and R. Vaßen, Gadolinium Zirconate/YSZ Thermal Barrier Coatings: Plasma Spraying, Microstructure, and Thermal Cycling Behavior, *J. Am. Ceram. Soc.*, 2014, **97**(12), p 4045-4051

81. I.V. Mazilin, L.K. Baldaev, D.V. Drobot, E.Y. Marchukov, and A.M. Akhmetgareeva, Composition and Structure of Coatings Based on Rare-Earth Zirconates, *Inorg. Mater.*, 2016, **52**(9), p 939-944

82. H. Zhao, C.G. Levi, and H.N.G. Wadley, Vapor Deposited Samarium Zirconate Thermal Barrier Coatings, *Surf. Coat. Technol.*, 2009, **203**, p 3157-3167

83. C. Wan, Z. Qu, A. Du, and W. Pan, Influence of B Site Substituent Ti on the Structure and Thermophysical Properties of A$_2$B$_2$O$_7$-Type Pyrochlore Gd$_2$Zr$_2$O$_7$, *Acta Mater.*, 2009, **57**(16), p 4782-4789

84. N.J. Hess, B.D. Begg, S.D. Conradson, D.E. McCready, P.L. Gassman, and W.J. Weber, Spectroscopic Investigations of the Structural Phase Transition in Gd$_2$(Ti$_{1-y}$Zr$_y$)$_2$O$_7$ Pyrochlores, *J. Phys. Chem. B*, 2002, **106**(18), p 4663-4677

85. F. Qun-bo, Z. Feng, W. Fu-chi, and L. Wang, Molecular Dynamics Calculation of Thermal Expansion Coefficient of a Series of Rare-Earth Zirconates, *Comput. Mater. Sci.*, 2009, **46**(3), p 716-719

86. M. Freling, M.J. Maloney, D.A. Litton, K.W. Schlichting, J.G. Smeggil, and D.B. Snow, *Thermal Barrier Coating Compositions, Processes for Applying Same and Articles Coated With Same*, U.S. Patent 7,455,913 (2008)

87. D.A. Litton, K.W. Schlichting, M. Freling, J.G. Smeggil, D.B. Snow, and M.J. Maloney, *Durable Reactive Thermal Barrier Coatings*, U.S. Patent 7,662,489 (2010)

88. S. Krämer, J. Yang, and C.G. Levi, Infiltration-Inhibiting Reaction of Gadolinium Zirconate Thermal Barrier Coatings with CMAS Melts, *J. Am. Ceram. Soc.*, 2008, **91**(2), p 576-583

89. J.M. Drexler, A.L. Ortiz, and N.P. Padture, Composition Effects of Thermal Barrier Coating Ceramics on Their Interaction with Molten Ca-Mg-Al–silicate (CMAS) Glass, *Acta Mater.*, 2012, **60**(15), p 5437-5447

90. D.L. Poerschke and C.G. Levi, Effects of Cation Substitution and Temperature on the Interaction Between Thermal Barrier Oxides and Molten CMAS, *J. Eur. Ceram. Soc.*, 2015, **35**(2), p 681-691

91. U. Schulz and W. Braue, Degradation of La$_2$Zr$_2$O$_7$ and Other Novel EB-PVD Thermal Barrier Coatings by CMAS (CaO-MgO-Al$_2$O$_3$-SiO$_2$) and Volcanic Ash Deposits, *Surf. Coat. Technol.*, 2013, **235**, p 165-173

92. B.R. Marple, J. Voyer, M. Thibodeau, D.R. Nagy, and R. Vassen, Hot Corrosion of Lanthanum Zirconate and Partially Stabilized Zirconia Thermal Barrier Coatings, *J. Eng. Gas Turbines Power*, 2004, **128**(1), p 144-152

93. M.H. Habibi, L. Wang, and S.M. Guo, Evolution of Hot Corrosion Resistance of YSZ, Gd$_2$Zr$_2$O$_7$, and Gd$_2$Zr$_2$O$_7$ + YSZ Composite Thermal Barrier Coatings in Na$_2$SO$_4$ + V$_2$O$_5$ at 1050 °C, *J. Eur. Ceram. Soc.*, 2012, **32**(8), p 1635-1642

94. C.G. Levi, Emerging Materials and Processes for Thermal Barrier Systems, *Curr. Opin. Solid State Mater. Sci.*, 2004, **8**(1), p 77-91

95. R.M. Leckie, S. Krämer, M. Rühle, and C.G. Levi, Thermochemical Compatibility Between Alumina and ZrO$_2$–GdO$_{3/2}$ Thermal Barrier Coatings, *Acta Mater.*, 2005, **53**(11), p 3281-3292

96. H. Zhao, M.R. Begley, A. Heuer, R. Sharghi-Moshtaghin, and H.N.G. Wadley, Reaction, Transformation and Delamination of

Samarium Zirconate Thermal Barrier Coatings, *Surf. Coat. Technol.*, 2011, **205**(19), p 4355-4365

97. M.J. Maloney, *Thermal Barrier Coating Systems and Materials*, U.S. Patent 6,177,200 (2001)

98. R. Subramanian, *Thermal Barrier Coating Having High Phase Stability*, U.S. Patent 6,387,539 (2002)

99. G. Dwivedi, V. Viswanathan, S. Sampath, A. Shyam, and E. Lara-Curzio, Fracture Toughness of Plasma-Sprayed Thermal Barrier Ceramics: Influence of Processing, Microstructure, and Thermal Aging, *J. Am. Ceram. Soc.*, 2014, **97**(9), p 2736-2744

100. Y. Zhang, L. Guo, X. Zhao, and F. Ye, Effects of Non-stoichiometry on the Mechanical Properties of $Nd_{2-x}Zr_{2+x}O_{7+x/2}$ (x = 0, 0.1, 0.2, 0.3, 0.4, 0.5) Ceramics, *Mater. Lett.*, 2014, **136**, p 157-159

101. L. Guo, M. Li, Y. Zhang, and F. Ye, Improved Toughness and Thermal Expansion of Non-stoichiometry $Gd2 - xZr2 + xO7 + x/2$ Ceramics for Thermal Barrier Coating Application, *J. Mater. Sci. Technol.*, 2016, **32**(1), p 28-33

102. M.P. Schmitt, J.L. Stokes, B.L. Gorin, A.K. Rai, D. Zhu, T.J. Eden, and D.E. Wolfe, Effect of Gd Content on Mechanical Properties and Erosion Durability of Sub-stoichiometric $Gd_2Zr_2O_7$, *Surf. Coat. Technol.*, 2017, **313**, p 177-183

103. R.M.R. Leckie, *Fundamental Issues Regarding the Implementation of Gadolinium Zirconate in Thermal Barrier Coatings*, University of California Santa Barbara, Santa Barbara, 2006

104. C. Wang, L. Guo, Y. Zhang, X. Zhao, and F. Ye, Enhanced Thermal Expansion and Fracture Toughness of Sc_2O_3-Doped $Gd_2Zr_2O_7$ Ceramics, *Ceram. Int.*, 2015, **41**(9, Part A), p 10730-10735

105. J.Y. Li, H. Dai, X.H. Zhong, Y.F. Zhang, X.F. Ma, J. Meng, and X.Q. Cao, Effect of the Addition of YAG (Y3Al5O12) Nanopowder on the Mechanical Properties of Lanthanum Zirconate, *Mater. Sci. Eng. A*, 2007, **460-461**, p 504-508

106. J.Y. Li, H. Dai, X.H. Zhong, Y.F. Zhang, X.F. Ma, J. Meng, and X.Q. Cao, Lanthanum Zirconate Ceramic Toughened by $BaTiO_3$ Secondary Phase, *J. Alloys Compd.*, 2008, **452**(2), p 406-409

107. Y. Zhang, J. Malzbender, D.E. Mack, M.O. Jarligo, X. Cao, Q. Li, R. Vaßen, and D. Stöver, Mechanical Properties of Zirconia Composite Ceramics, *Ceram. Int.*, 2013, **39**(7), p 7595-7603

108. L. Ma, W. Ma, X. Sun, L. Ji, J. Liu, and K. Hang, Microstructures and Mechanical Properties of $Gd_2Zr_2O_7$/ZrO_2(3Y) Ceramics, *J. Alloys Compd.*, 2015, **644**, p 416-422

109. Y. Zhang, L. Guo, X. Zhao, C. Wang, and F. Ye, Toughening Effect of Yb_2O_3 Stabilized ZrO_2 Doped in $Gd_2Zr_2O_7$ Ceramic for Thermal Barrier Coatings, *Mater. Sci. Eng. A*, 2015, **648**, p 385-391

110. M. Li, L. Guo, and F. Ye, Phase Structure and Thermal Conductivities of Er_2O_3 Stabilized ZrO_2 Toughened $Gd_2Zr_2O_7$ Ceramics for Thermal Barrier Coatings, *Ceram. Int.*, 2016, **42**(15), p 16584-16588

111. N.S. Jacobson, *Thermodynamic Properties of Some Metal Oxide-Zirconia Systems*, NASA-Lewis Research Center, Cleveland, 1989

112. X.Q. Cao, R. Vassen, W. Jungen, S. Schwartz, F. Tietz, and D. Stöver, Thermal Stability of Lanthanum Zirconate Plasma-Sprayed Coating, *J. Am. Ceram. Soc.*, 2001, **84**(9), p 2086-2090

113. Z. Xu, X. Zhong, J. Zhang, Y. Zhang, X. Cao, and L. He, Effects of Deposition Conditions on Composition and Thermal Cycling Life of Lanthanum Zirconate Coatings, *Surf. Coat. Technol.*, 2008, **202**(19), p 4714-4720

114. E. Bakan, D.E. Mack, G. Mauer, R. Mücke, and R. Vaßen, Porosity-Property Relationships of Plasma-Sprayed $Gd_2Zr_2O_7$/YSZ Thermal Barrier Coatings, *J. Am. Ceram. Soc.*, 2015, **98**(8), p 2647-2654

115. E. Bakan, *Yttria-Stabilized Zirconia/Gadolinium Zirconate Double-Layer Plasma-Sprayed Thermal Barrier Coating Systems (TBCs)*, Ph.D. Thesis, Ruhr-Universität Bochum (2015)

116. K.E. Sickafus, L. Minervini, R.W. Grimes, J.A. Valdez, M. Ishimaru, F. Li, K.J. McClellan, and T. Hartmann, Radiation Tolerance of Complex Oxides, *Science*, 2000, **289**(5480), p 748-751

117. J.M. Drexler, C.-H. Chen, A.D. Gledhill, K. Shinoda, S. Sampath, and N.P. Padture, Plasma Sprayed Gadolinium Zirconate Thermal Barrier Coatings that are Resistant to Damage by Molten Ca-Mg-Al-silicate glass, *Surf. Coat. Technol.*, 2012, **206**(19-20), p 3911-3916

118. G. Suresh, G. Seenivasan, M.V. Krishnaiah, and P.S. Murti, Investigation of the Thermal Conductivity of Selected Compounds of Gadolinium and Lanthanum, *J. Nucl. Mater.*, 1997, **249**(2-3), p 259-261

119. C. Wang, *Experimental and Computational Phase Studies of the ZrO_2-Based Systems for Thermal Barrier Coatings*, Universität Stuttgart, Stuttgart, 2006

120. J. Wang, S. Bai, H. Zhang, and C. Zhang, The Structure, Thermal Expansion Coefficient and Sintering Behavior of Nd^{3+}-Doped $La_2Zr_2O_7$ for Thermal Barrier Coatings, *J. Alloys Compd.*, 2009, **476**(1-2), p 89-91

121. W. Ma, X. Li, Y. Yin, H. Dong, Y. Bai, J. Liu, D. Nan, and J. Wang, The Mechanical and Thermophysical Properties of $La_2(Zr_{1-x}Ce_x)_2O_7$ Ceramics, *J. Alloys Compd.*, 2016, **660**, p 85-92

122. R. Vaßen, X. Cao, F. Tietz, D. Basu, and D. Stöver, Zirconates as New Materials for Thermal Barrier Coatings, *J. Am. Ceram. Soc.*, 2000, **83**(8), p 2023-2028

123. O. Fabrichnaya, R. Wulf, M.J. Kriegel, G. Savinykh, M. Dopita, J. Seidel, H.C. Heitz, O. Nashed, U. Gross, and H.J. Seifert, Thermophysical Properties of Pyrochlore and Fluorite Phases in the $Ln_2Zr_2O_7$-Y_2O_3 Systems (Ln = La, Nd, Sm): 2. Comparison of Conventionally Sintered and SPS Samples in the Systems $Nd_2Zr_2O_7$-Y_2O_3 and $Sm_2Zr_2O_7$-Y_2O_3, *J. Alloys Compd.*, 2015, **625**, p 200-207

124. G. Suresh, G. Seenivasan, M.V. Krishnaiah, and P.S. Murti, Investigation of the Thermal Conductivity of Selected Compounds of Lanthanum, Samarium and Europium, *J. Alloys Compd.*, 1998, **269**(1-2), p L9-L12

125. Z. Qu, C. Wan, and W. Pan, Thermal Expansion and Defect Chemistry of MgO-Doped $Sm_2Zr_2O_7$, *Chem. Mater.*, 2007, **19**(20), p 4913-4918

126. H.-S. Zhang, K. Sun, Q. Xu, F.-C. Wang, and L. Liu, Preparation and Thermal Conductivity of $Sm_2(Zr_{0.6}Ce_{0.4})_2O_7$ Ceramic, *J. Mater. Eng. Perform.*, 2009, **18**(8), p 1140

127. O. Fabrichnaya, M.J. Kriegel, D. Pavlyuchkov, J. Seidel, A. Dzuban, G. Savinykh, and G. Schreiber, Heat Capacity for the $Eu_2Zr_2O_7$ and Phase Relations in the ZrO_2-Eu_2O_3 System: Experimental Studies and Calculations, *Thermochim. Acta*, 2013, **558**, p 74-82

128. X. Wang, L. Guo, H. Zhang, S. Gong, and H. Guo, Structural Evolution and Thermal Conductivities of $(Gd_{1-x}Yb_x)_2Zr_2O_7$ (x = 0, 0.02, 0.04, 0.06, 0.08, 0.1) Ceramics for Thermal Barrier Coatings, *Ceram. Int.*, 2015, **41**(10, Part A), p 12621-12625

129. K.W. Schlichting, N.P. Padture, and P.G. Klemens, Thermal Conductivity of Dense and Porous Yttria-Stabilized Zirconia, *J. Mater. Sci.*, 2001, **36**(12), p 3003-3010

130. H. Hayashi, T. Saitou, N. Maruyama, H. Inaba, K. Kawamura, and M. Mori, Thermal Expansion Coefficient of Yttria Stabilized Zirconia for Various Yttria Contents, *Solid State Ion.*, 2005, **176**(5-6), p 613-619